NUWC-NPT Technical Report 10,833
8 March 1995

Space-Time Characteristics of the Turbulent Flow Energy in a Viscoelastic Medium Using Noninvasive Passive Imaging

Norman L. Owsley
Mohamed H. Ahmed
Andrew J. Hull
Submarine Sonar Department

James Kassal
Analysis and Technology Inc.

Naval Undersea Warfare Center Division
Newport, Rhode Island

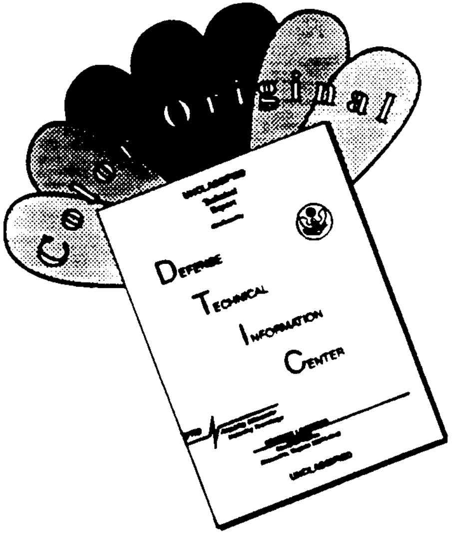
Original
Defense
Technical
Information
Center

REPORT DOCUMENTATION PAGE

Form Approved
OMB No. 0704-0188

1. AGENCY USE ONLY (Leave Blank)

2. REPORT DATE

8 March 1995

3. REPORT TYPE AND DATES COVERED

Progress

4. TITLE AND SUBTITLE

Space-Time Characteristics of the Turbulent Flow Energy in a Viscoelastic Medium Using Noninvasive Passive Imaging

5. FUNDING NUMBERS

6. AUTHOR(S)

Norman L. Owsley, Mohamed H. Ahmed, Andrew J. Hull
NUWC Detachment New London

James Kassal
Analysis and Technology Inc

7. PERFORMING ORGANIZATION NAME(S) AND ADDRESS(ES)

Naval Undersea Warfare Center
Detachment New London
New London, Connecticut 06320

8. PERFORMING ORGANIZATION REPORT NUMBER

TR 10,833

9. SPONSORING/MONITORING AGENCY NAME(S) AND ADDRESS(ES)

Office of Naval Research
800 North Quincy Street
Arlington, VA 22217

Program Executive Office
USW/ASTO
2531 Jefferson Davis Highway
Arlington, VA 22242

10. SPONSORING/MONITORING AGENCY REPORT NUMBER

11. SUPPLEMENTARY NOTES

12a. DISTRIBUTION/AVAILABILITY STATEMENT

Approved for public release; distribution is unlimited.

12b. DISTRIBUTION CODE

13. ABSTRACT (Maximum 200 words)

This report describes the technology required for noninvasive passive imaging of the turbulent flow energy of space-time signals in a viscoelastic medium. The need for such technology emerges from the field of biomedicine, where low cost noninvasive techniques are necessary to accurately diagnose heart disease. A sensor that can detect extremely low energy levels, such as those encountered in a stenosed artery, is investigated. An experiment that consists of a urethane solid containing a partially blocked embedded surgical tube is described. Measurements of turbulence-induced energy levels are included in both the spatial-frequency domain and the wavenumber-frequency domain. Modeling of continuous sources using two different beamformers is addressed. Also presented are recommendations for future studies.

14. SUBJECT TERMS

Auscultation, Biomedicine, Flow-Induced Signals, Heart Disease Diagnosis, Imaging, Noninvasive Imaging, Passive Imaging, Space-Time Signals, Viscoelastic Medium

15. NUMBER OF PAGES

66

16. PRICE CODE

17. SECURITY CLASSIFICATION OF REPORT

UNCLASSIFIED

18. SECURITY CLASSIFICATION OF THIS PAGE

UNCLASSIFIED

19. SECURITY CLASSIFICATION OF ABSTRACT

UNCLASSIFIED

20. LIMITATION OF ABSTRACT

SAR

TABLE OF CONTENTS

LIST OF ILLUSTRATIONS

LIST OF TABLES

SPACE-TIME CHARACTERISTICS OF THE TURBULENT FLOW ENERGY IN A VISCOELASTIC MEDIUM USING NONINVASIVE PASSIVE IMAGING

CHAPTER 1. INTRODUCTION

Attempts to noninvasively diagnose coronary artery disease (Akay et al., 1992) and intracranial vascular lesions and aneurysms (Abiko et al., 1994) by passive listening (auscultation) for the effects of blood flow turbulence have been reported in the recent literature. The potential for these techniques to result in low cost, mass screening examinations is considerable. However, the feasibility of such noninvasive detection of human arterial disease for other than a near-surface artery depends on the ability to discriminate signals with a very low energy level from high level background masking interference and physiologically produced noise. It is proposed here to enhance the desired signal-to-noise ratio (SNR) through the use of an array of noninvasive vibroacoustic sensors placed on the body surface. It is suggested that the wave lengths for vibrations, which occur in the frequency decade from 100 to 1000 Hz (Verberg, 1983), are appropriate for spatially discriminating signals from noise on the basis of joint space-time signal processing. The space-time signals of interest result from (blood) turbulence-induced forces normal and parallel to a diseased artery internal wall, which, in turn, couple as wave energy to the body surface by means of a time-varying spatial vibration field. This space-time field describes the energy propagation in the viscoelastic body medium. It is proposed that the three-dimensional vibration field can be sensed by an array of transducers placed on the skin. The spatial discrimination properties of the array would be used as a generalized focusing "antenna" to enhance the SNR relative to that which could be achieved with a single sensor (Owsley et al., 1985; Owsley, 1994).

A blood flow turbulence-induced murmur can be discriminated from masking background sound in the temporal, spectral, and spatial domains. For example, temporal discrimination against background noise in auscultation for coronary artery disease (CAD) is based on the simple fact that sounds characterizing occlusive coronary stenosis occur during diastole (Akay et al., 1990). Energy from stenosed coronary arteries must therefore be extracted from a background noise environment that results from the rapid filling of the ventricle chambers, including the first and second heart sounds. Moreover, it has been suggested that resonance effects in arteries excited by blood flow produce characterizable, albeit low level, sonic signatures (Wang, 1990). Double resonant frequencies below 400 Hz are predicted, whereas experimentally CAD-related resonant energy as high as 1100 Hz due to turbulent blood flow caused by lesions on the inner wall of an occluded artery is reported (Akay et al., 1992). In addition, quantitative blood flow rate may be measurable in the absence of highly turbulent flow-induced resonance by estimating the level and cutoff frequencies of the broadband energy produced by low level turbulence, which is, in turn, related to the diameter of the stenotic carotid segment (Lees and Kistler, 1978). In this study, it is suggested that a key to reliable detection, identification, and location of arterial lesions and aneurysms may very well lie in the *spatial* domain. It is thus proposed that the detection of the type and location of both normal and pathologic blood flow vibration-induced acoustic and nonacoustic energy can potentially be accomplished through simultaneous filtering and combining of the outputs of a spatially diverse array of vibro-acoustic transducers.

For CAD, the signal levels produced by the effects of relatively small coronary artery blood flow rates are substantially below the levels produced by nearby flow activity, such as ventricle refilling during diastole. Moreover, the ambient environmental noise produced by noncardiac functions is a known inhibitor to low level sound detection and diagnosis. It is well known that the audible sonic field produced by the cardiac cycle exhibits a high degree of spatial variability (Epstein, 1991). The traditional auscultation in phonocardiography involves the placement of a single vibro-acoustic transducer anywhere in the area of energy propagation associated with high quality transmission from a particular region of the heart. In contrast, multiple auscultation point (MAP) space-time phonocardiography proposes to receive energy simultaneously at an array of transducers and through the application of modern space-time signal processing technology to provide:

(a) a maximum SNR *estimate of the waveform* produced by the turbulent blood flow activity in a specific region of the body by coherently combining the spatially diverse samples of the vibration field, thereby enhancing the desired signal and discriminating against interfering components to the measured space-time field and

(b) a *spatially and spectrally resolved image of the turbulent-flow-induced spatially extended vibratory energy source* for either a narrowband (resonant) phenomenon or a spectrally wideband phenomenon (e.g., low intensity level turbulent flow activity and artifacts such as stenotic valve clicks and prosthetic valve/vessel failure points.

Enhanced SNR waveform estimation is critical to low error rate detection algorithms for low level sonic activity. High resolution imaging of energy fields due to turbulent fluid jets would be invaluable for the prognosis and treatment of lesions and aneurysms. The combination of these two capabilities has the potential for a relatively low cost alternative to invasive procedures and in particular to catheterization.

This report first defines the experimental apparatus and array transducer used to measure the viscoelastic properties that support wave propagation in the body resulting from turbulent-flow-induced vibrations. Next, a proof-of-concept (POC) experiment that establishes the feasibility of the proposed MAP concept using frequency-wavenumber analysis is described, and an attempt at the interpretation of the experimental results in terms of propagating shear and surface waves is examined. The potential for three-dimensional high resolution imaging is validated through a numerical simulation of the simulated space-time vibrational energy field. Finally, work is proposed that constitutes the basis for the development of a commercially viable clinical application of the MAP concept to very low cost, noninvasive mass diagnostic screening.

CHAPTER 2. EXPERIMENTAL APPARATUS

2.1. LABORATORY CONFIGURATION

The experimental apparatus consists of a 10.9 by 6.1 by 4.0 inch rectangular Hexcel 195-RE urethane block with embedded surgical tubing at a depth of 0.69 inch (figure 2.1). Inside the surgical tubing is a cylindrical nylon blockage that is 1.0 inch long with two U-shaped cuts, as shown in figure 2.2. The outer diameter of the blockage is 0.125 inch and the inner diameter is 0.043 inch. The blockage is designed to convert an incoming laminar flow field into a turbulent flow field. An elevated 50-gallon upper reservoir feed tank is located next to the urethane block and connected to the surgical tubing. The water drains from the upper reservoir through the urethane block and into a calibrated flask located below the block (figure 2.3). The fluid velocity can be changed by varying the head pressure of the 50-gallon tank. One sensor was positioned at a fixed location directly above the blockage and the other was placed at various locations downstream of the blockage during the course of the experiment.

2.2. SENSOR

The sensor used in this experiment is a polyvinylidene fluoride (PVDF) motion sensor (Kassal et al., 1994). The PVDF piezoelectric polymer produces charges of equal magnitude and opposite polarity on opposite surfaces when a mechanical strain is imposed on the material. The size of the surface charge is proportional to the size of the strain. The sensor is designed for use in cardiac auscultation, although it measures motion rather than acoustic pressure. It is 1 inch by 1.25 inches and the active (measurement) size of the sensor is 1 inch by 1 inch. It consists of two rectangular thin-film PVDF elements, a flexible substrate, a miniature three-conductor electrical connector, a moisture barrier that also acts as a protective coating, and a connector bib to keep the cable connector receptacles clean. Hydrogel adhesive is applied between the sensor and the measurement location to ensure good mechanical contact. The signal from the sensor is passed to a differential amplifier to increase the signal and then into an HP3562A signal analyzer.

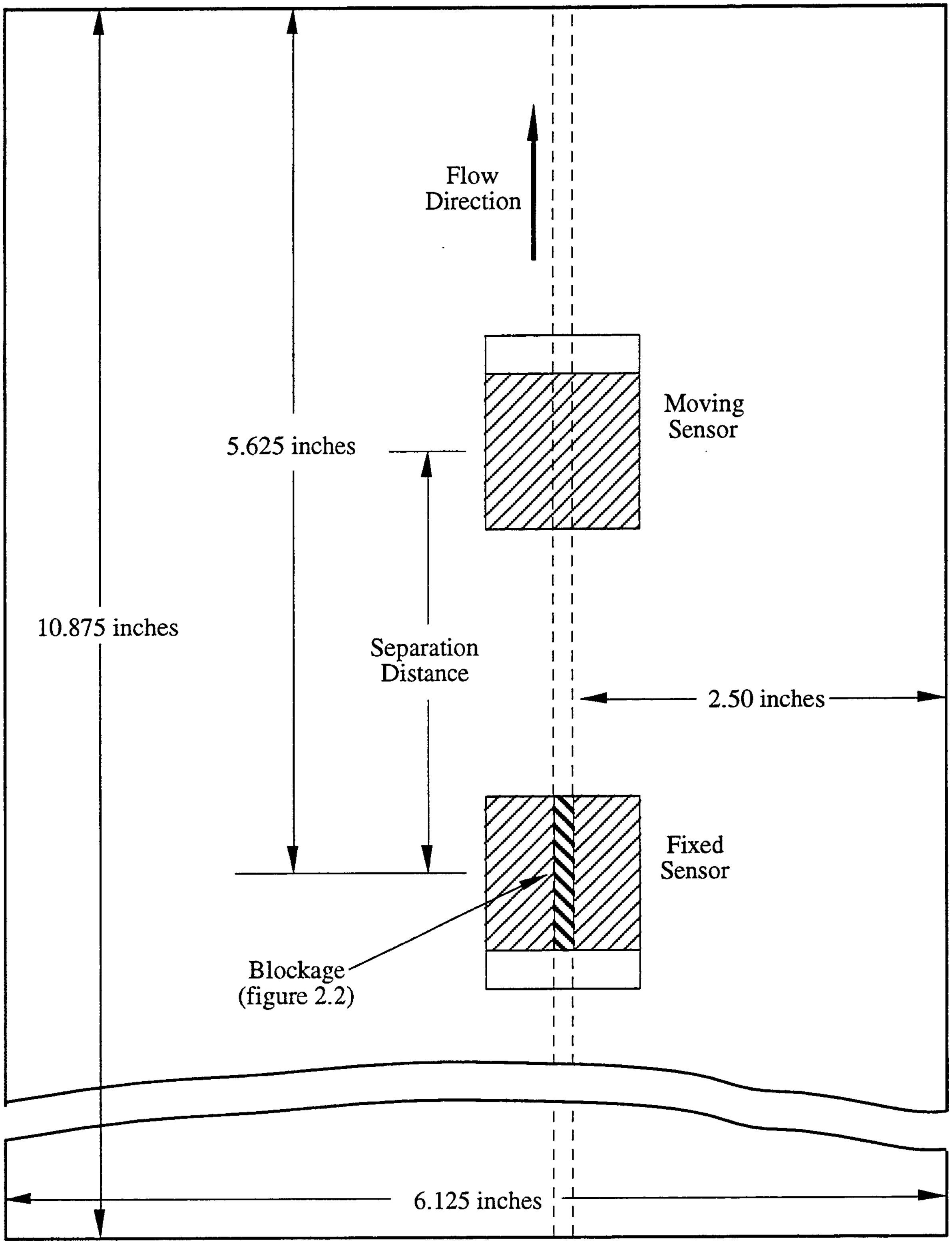

Figure 2.1. Urethane Block With Sensors

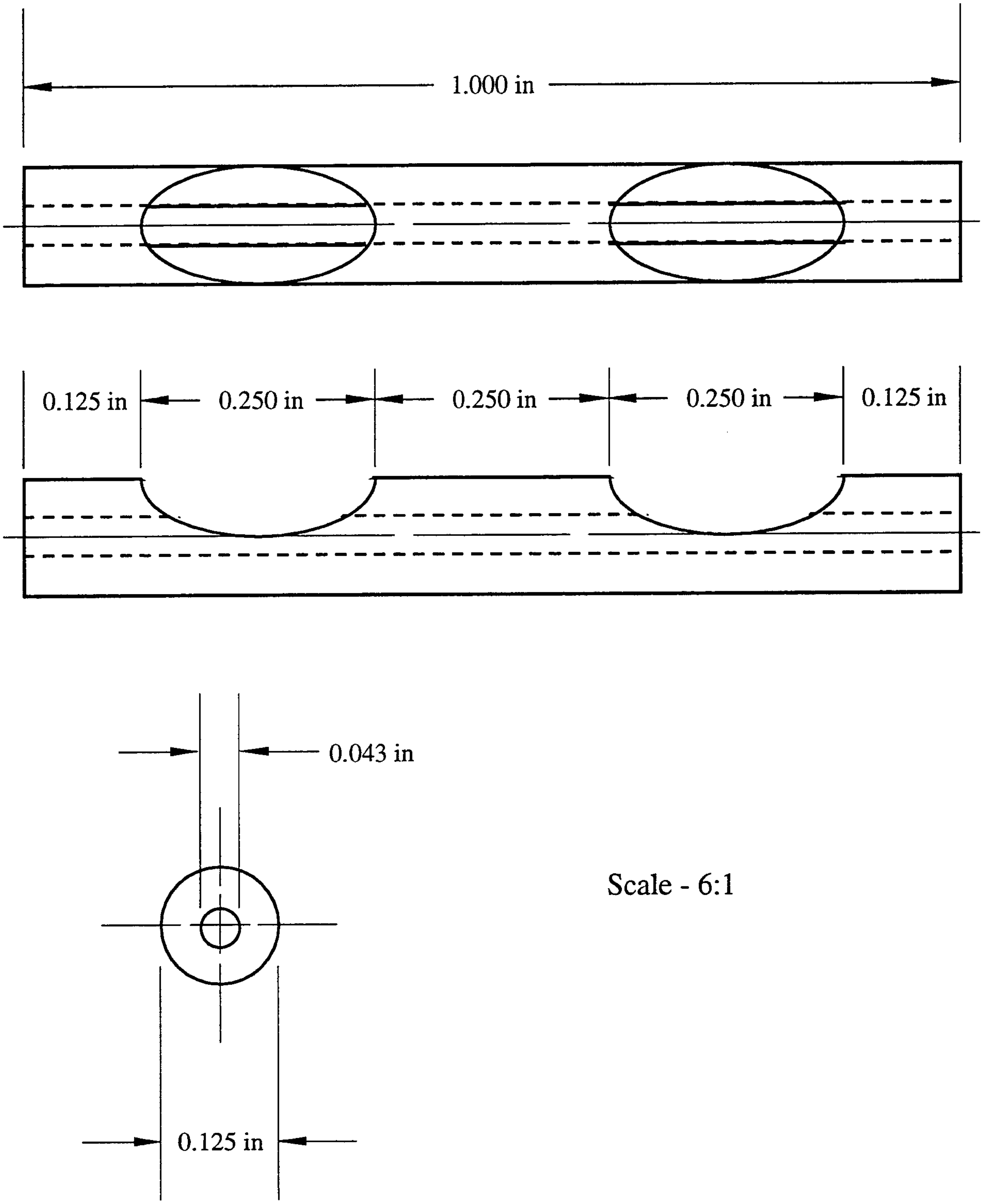

Scale - 6:1

Figure 2.2. Nylon Blockage

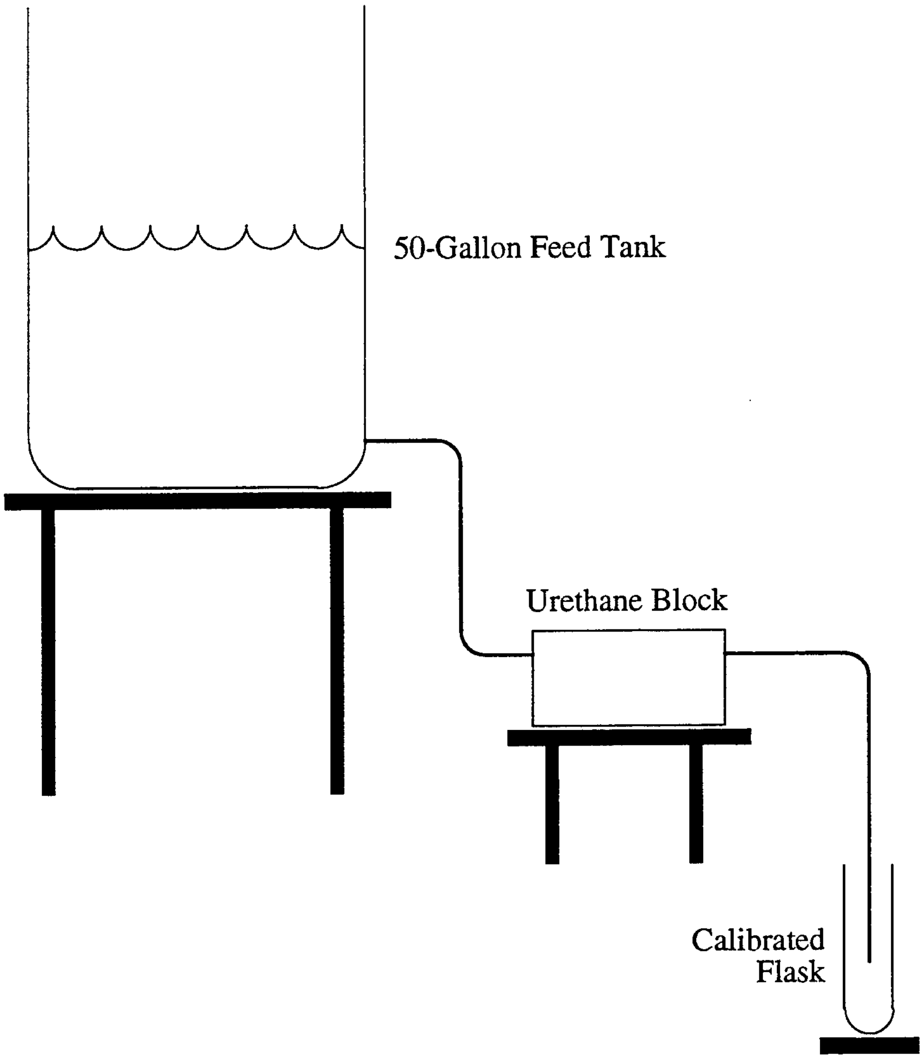

Figure 2.3. Laboratory Configuration

CHAPTER 3. EXPERIMENTAL RESULTS AS AN INITIAL PROOF OF CONCEPT (POC)

3.1. INTRODUCTION

An initial proof-of-concept experiment was performed on the laboratory apparatus described in chapter 2. The results were obtained by first measuring frequency domain transfer functions between a stationary sensor and a relocatable sensor positioned at 15 locations and then by applying a Fourier transform to the spatial domain data for conversion into the wavenumber domain. This process is equivalent to that of a farfield beamformer whose focal point is at infinity. These frequency-wavenumber ($k\omega$) data surfaces are displayed primarily as wavenumber cuts at constant frequency. Wave motion is identified on these wavenumber cuts, and the corresponding apparent wave speed is calculated. These wave speeds are then compared to theoretical values determined from material property measurements. The energy levels present in the sidelobe structures of the beam are also analyzed.

3.2. MATERIAL MEASUREMENTS

The Hexcel 195-RE urethane and the surgical tubing were tested using the Metravib Viscoanalyseur in order to determine their dynamic material properties. The Viscoanalyseur is a material testing machine designed to measure the complex compressional and shear moduli as a function of frequency and temperature (Metravib, 1989). Table 3.1 is a listing of the compressional modulus and table 3.2 is a listing of the shear modulus of Hexcel 195-RE urethane. Table 3.3 lists the compressional modulus and table 3.4 lists the shear modulus of the surgical tubing. All four tables show measurements made at 20 degrees C. For completeness, we note that using the compressional and shear moduli to calculate a value for Poisson's ratio yields a number ranging from 2 to 4, a physically unrealizable value. It is believed that this error resides in the measured values for the compressional modulus. The Materials Laboratory at NUWC Detachment New London is addressing the issue of incompatible Poisson's ratios. The density of Hexcel 195-RE urethane is 930 kg/m^3.

Table 3.1. Compressional Modulus of Hexcel 195-RE Urethane Measured With the Viscoanalyseur

Frequency (Hz)	Real (E) (N/m^2)	Imaginary(E) (N/m^2)
5.0	4.90×10^5	1.25×10^5
54.5	6.29×10^5	3.80×10^5
104.0	8.26×10^5	3.47×10^5
153.6	9.03×10^5	3.95×10^5
202.9	9.68×10^5	4.28×10^5
252.5	10.10×10^5	4.59×10^5
301.9	10.50×10^5	4.89×10^5
351.1	10.70×10^5	5.17×10^5
400.6	10.80×10^5	5.39×10^5
451.3	10.50×10^5	5.67×10^5
500.0	9.72×10^5	6.30×10^5

Table 3.2. Shear Modulus of Hexcel 195-RE Urethane Measured With the Viscoanalyseur

Frequency (Hz)	Real (G) (N/m^2)	Imaginary(G) (N/m^2)
5.0	1.04×10^5	0.149×10^5
54.5	1.32×10^5	0.313×10^5
104.0	1.43×10^5	0.386×10^5
153.6	1.52×10^5	0.438×10^5
202.9	1.59×10^5	0.466×10^5
252.5	1.65×10^5	0.505×10^5
301.9	1.69×10^5	0.537×10^5
351.1	1.73×10^5	0.557×10^5
400.6	1.67×10^5	0.555×10^5
451.3	1.63×10^5	0.618×10^5
500.0	1.45×10^5	0.698×10^5

Table 3.3. Compressional Modulus of Surgical Tubing Measured With the Viscoanalyseur

Frequency (Hz)	Real (*E*) (N/m^2)	Imaginary(*E*) (N/m^2)
5.0	69.4×10^5	4.59×10^5
54.5	76.1×10^5	6.03×10^5
104.0	77.3×10^5	7.13×10^5
153.6	77.2×10^5	9.21×10^5
202.9	80.2×10^5	8.03×10^5
252.5	81.3×10^5	8.29×10^5
301.9	82.4×10^5	8.43×10^5
351.1	83.4×10^5	8.72×10^5
400.6	84.3×10^5	8.97×10^5
451.3	85.1×10^5	9.26×10^5
500.0	85.8×10^5	9.68×10^5

Table 3.4. Shear Modulus of Surgical Tubing Measured With the Viscoanalyseur

Frequency (Hz)	Real (*G*) (N/m^2)	Imaginary(*G*) (N/m^2)
5.0	7.45×10^5	0.576×10^5
54.5	7.93×10^5	0.843×10^5
104.0	7.94×10^5	1.010×10^5
153.6	8.02×10^5	1.150×10^5
202.9	8.19×10^5	1.160×10^5
252.5	8.29×10^5	1.290×10^5
301.9	8.39×10^5	1.360×10^5
351.1	8.43×10^5	1.380×10^5
400.6	8.48×10^5	1.500×10^5
451.3	8.45×10^5	1.570×10^5
500.0	8.28×10^5	1.690×10^5

Based on these shear modulus measurements note that the shear wave speed in the urethane is 10 to 14 m/s in the frequency region of 0 to 500 Hz. The shear wave speed of typical tissue is 13 m/s at 1000 Hz (Verburg, 1983) although the dispersive properties of the shear wave in tissue are more severe (at lower frequencies) than the urethane used in this test. Because the compressional wave speed in the urethane is difficult to calculate due to the uncertainty of the measured compressional modulus, the measurements of the POC experiment are shown (below) to be shear wave dominant and compressional energy to be negligible.

3.3. FREQUENCY-SPATIAL DOMAIN MEASUREMENTS

The frequency-spatial domain measurements were made using an HP3562A dynamic signal analyzer. The analyzer converts the raw data from the time domain to the frequency domain. The measurements were made using two different measurement types: power spectral density and transfer function. Power spectral density is a measure of the energy of a single sensor, and the transfer function is a measure of the relative amplitude and phase in two sensors. Both measurements are made with respect to frequency. We define

$$G_{xx}(f) = \overline{F_x(f)F_x^*(f)} \ , \tag{3.1a}$$

$$G_{yy}(f) = \overline{F_y(f)F_y^*(f)} \ , \tag{3.1b}$$

and

$$G_{xy}(f) = \overline{F_x(f)F_y^*(f)} \ , \tag{3.1c}$$

where $G_{xx}(f)$ and $G_{yy}(f)$ are the autopower spectrum densities (APSD) of channel x and y, respectively; $G_{xy}(f)$ is the crosspower spectrum density (CPSD); $F_x(f)$ and $F_y(f)$ are the linear complex spectra of the waveforms $f_x(t)$ and $f_y(t)$, respectively; $F_x^*(f)$ and $F_y^*(f)$ are the complex conjugate of the linear spectrum; f is the frequency; and the bar above the right-hand side denotes a time average. The transfer function between channels x and y is defined as

$$H_{xy}(f) = \frac{G_{xy}(f)}{G_{xx}(f)} = \frac{\overline{F_x(f)F_y^*(f)}}{\overline{F_x(f)F_x^*(f)}} . \tag{3.2}$$

Additionally, the magnitude-squared (MSC) coherence function between channels x and y is defined as

$$\gamma^2 = \frac{G_{xy}(f)G_{xy}^*(f)}{G_{xx}(f)G_{yy}(f)} . \tag{3.3}$$

Figure 3.1 is a plot of the APSD of a sensor pad directly above the blockage. The solid line shows data taken with the flow and the dashed line shows data without flow. Note that at some frequencies there is almost a 20-dB SNR. Figure 3.2 plots the transfer function between sensors whose phase centers are separated by 1.09 inches. Because the distance from the phase center to the edge of each sensor is approximately 0.5 inch, figure 3.2 depicts the sensors' placement as being almost contiguous. The first sensor in figure 3.2 was located directly above the blockage and the second sensor was located downstream. Although the noise flow defined by the no-flow condition is not shown in this or the subsequent transfer functions, it is at an approximately -15-dB level in the magnitude plot of the transfer functions. Figure 3.3 is a plot of the transfer function between sensors whose phase centers are separated by 2.75 inches. Figure 3.4 is a plot of the transfer function between sensors whose phase centers are separated by 4.50 inches. In figures 3.3 and 3.4, the second sensor was moved downstream and the first remained over the blockage. The phase angle plots in figures 3.2, 3.3, and 3.4 show well-defined propagating energy content. Figures 3.5, 3.6, and 3.7 are plots of the MSC functions with sensor phase centers separated by 1.09, 2.75, and 4.50 inches, respectively. Although the coherence decreases as the measurement distance from the blockage increases, the signal is still highly coherent at 36 tube diameters downstream. All the data shown here were taken using a frequency range of 0 to 1000 Hz. The 500- to 1000- Hz portion of the data is not shown because the sensor is spatially averaging the high frequency content and coherent energy structures are removed. A smaller sensor will not produce this effect. For all of the measurements, the flow rate was 0.00348 liters/second, which has a corresponding Reynolds number of 1400. Although this value is below the Reynolds number for turbulent flow in a pipe, the flow field around the blockage will be turbulent due to the change in area caused by the blockage.

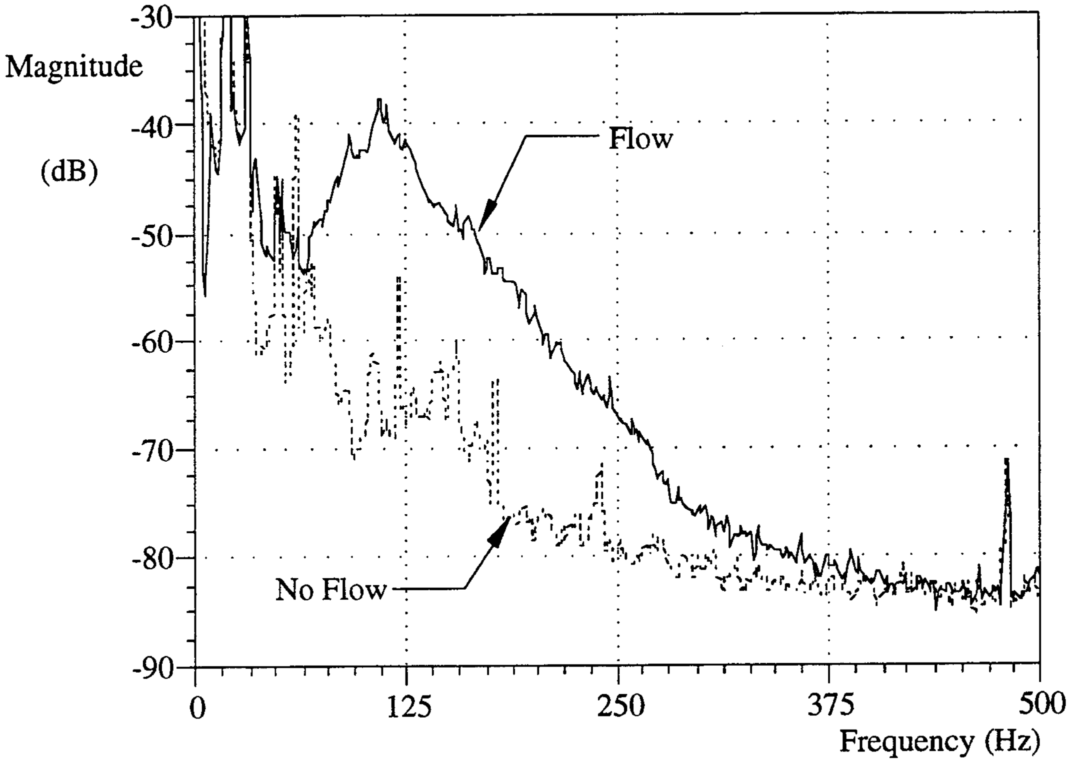

Figure 3.1. Power Spectrum of Sensor Over Blockage

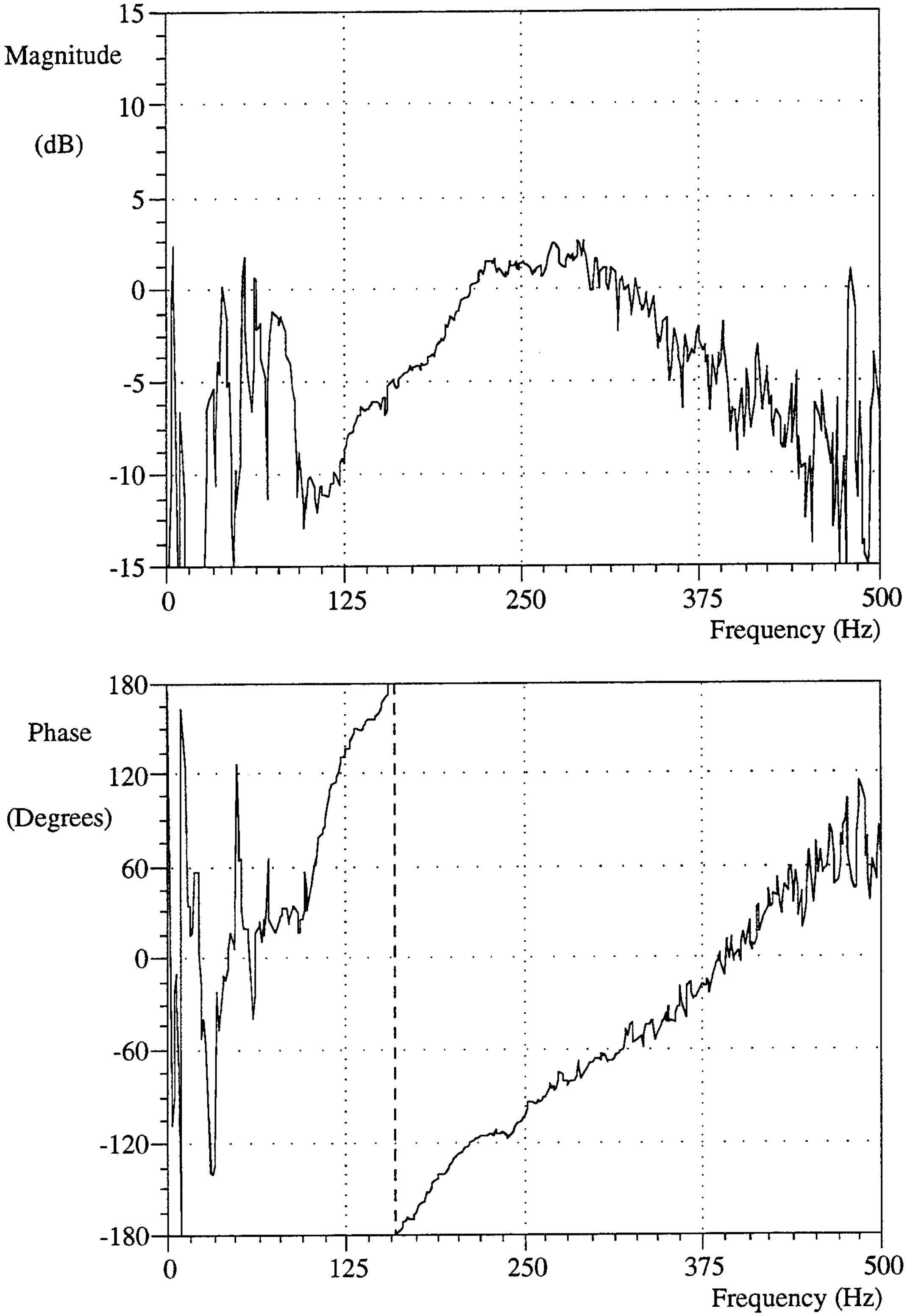

Figure 3.2. Transfer Function Between Sensors With Phase Centers Separated by 1.09 Inches

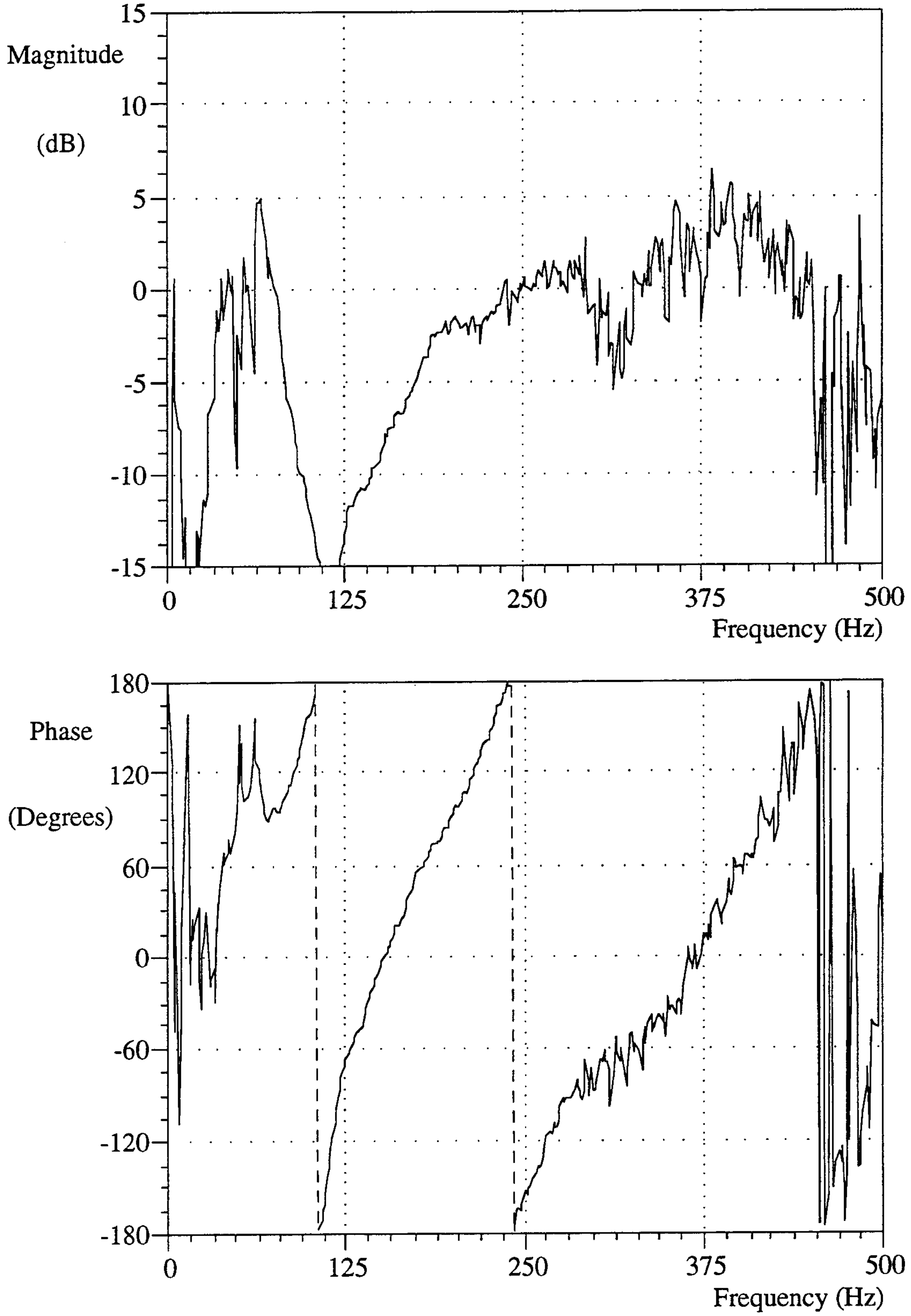

Figure 3.3. Transfer Function Between Sensors
With Phase Centers Separated by 2.75 Inches

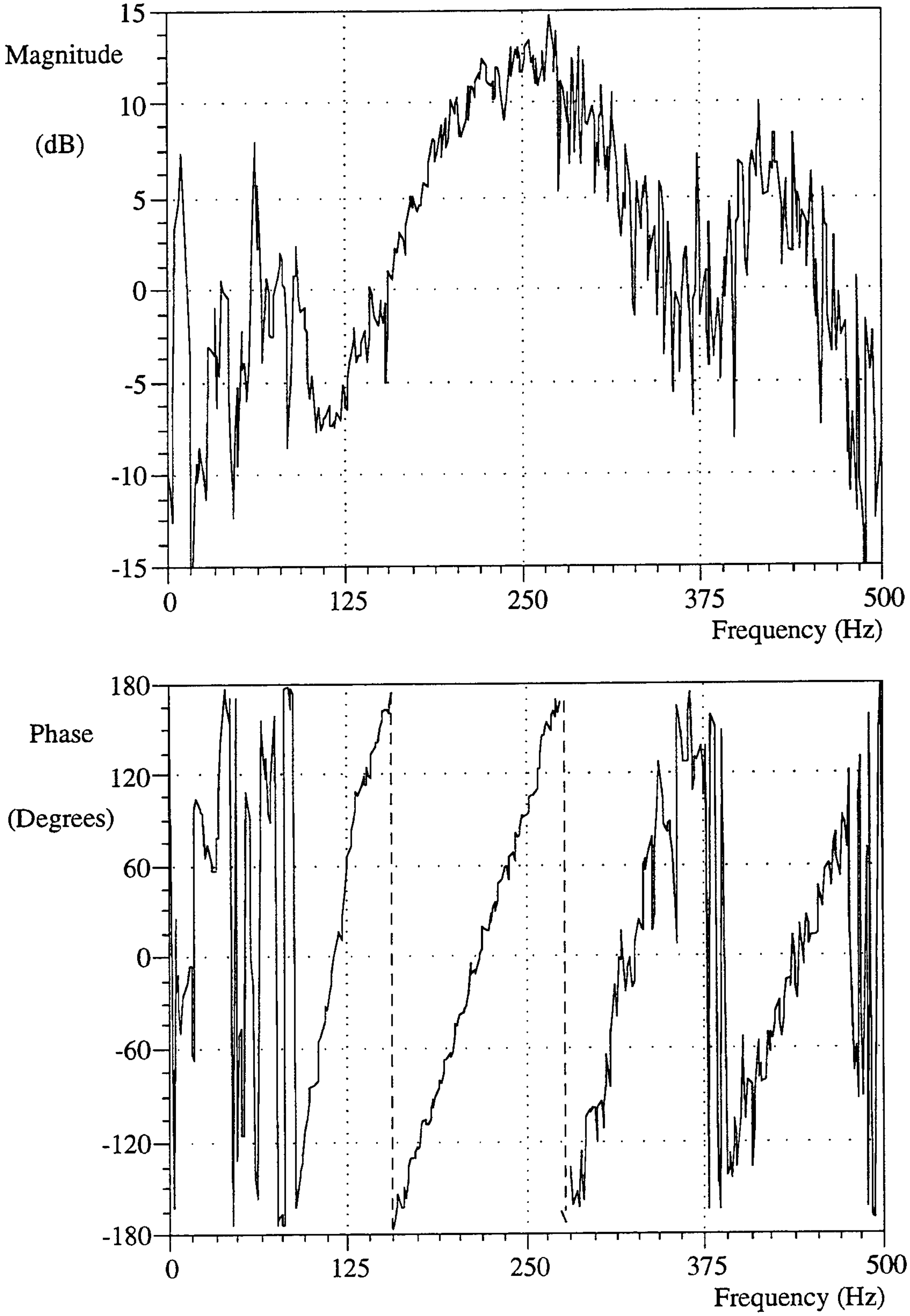

Figure 3.4. Transfer Function Between Sensors
With Phase Centers Separated by 4.50 Inches

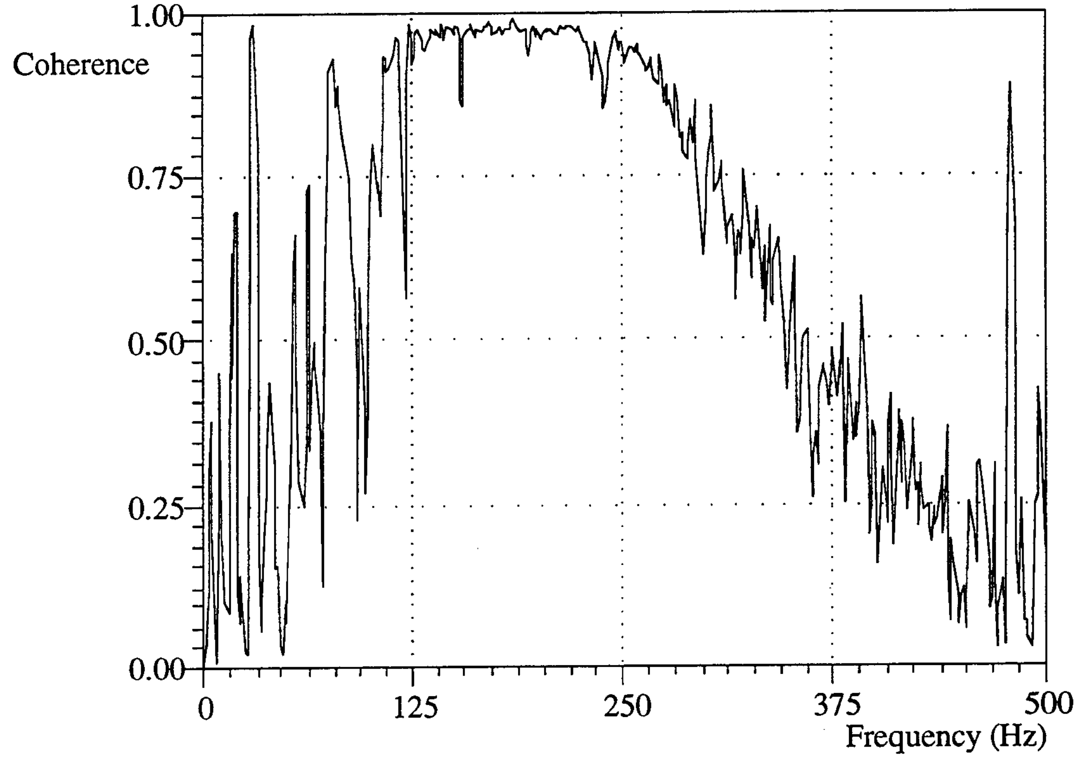

Figure 3.5. Coherence Between Sensors With
Phase Centers Separated by 1.09 Inches

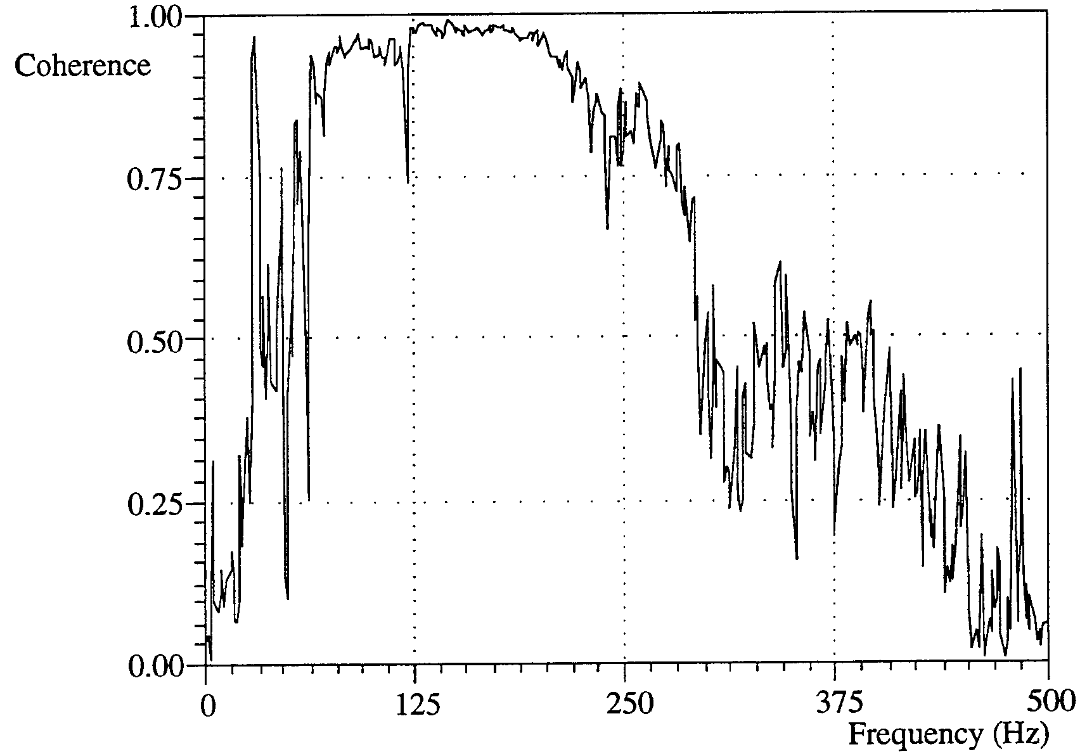

Figure 3.6. Coherence Between Sensors With
Phase Centers Separated by 2.75 Inches

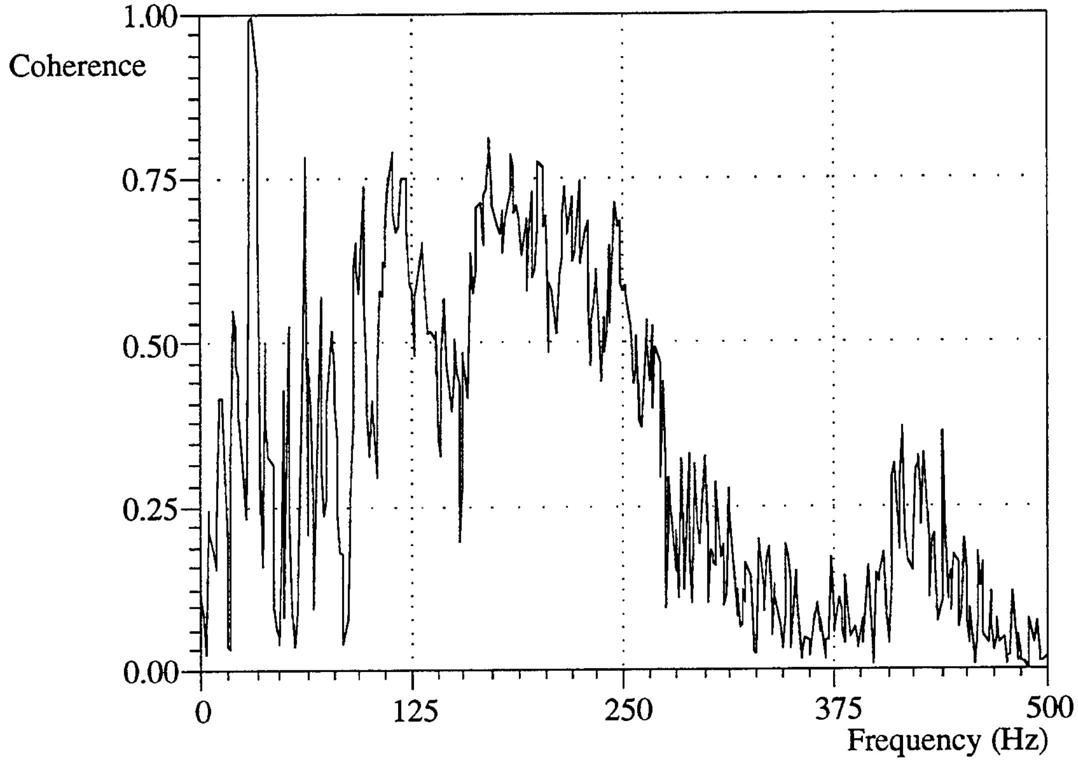

Figure 3.7. Coherence Between Sensors With Phase Centers Separated by 4.50 Inches

3.4. TRANSFORMATION FROM SPATIAL TO WAVENUMBER DOMAIN

The wavenumber domain allows the display of data that are dominated by several waves. As described above, the data, collected at each sensor channel in the form of a frequency domain transfer function of the downstream sensor divided by the stationary sensor above the blockage, are transformed from the spatial domain into the wavenumber domain by means of a discrete spatial Fourier transform at each frequency. This is the same process that a conventional beamformer (CBF) uses to detect propagating farfield-source planar wave energy.

The discrete Fourier transform originates with the Fourier integral, which converts a continuous function from the spatial (x) domain (meters) to the wavenumber (k) domain (radians/meter) (Corcos, 1963; Bradshaw, 1971; Smol'yakov and Tkachenko, 1983):

$$H(k) = \frac{1}{2\pi} \int_{-\infty}^{+\infty} h(x) e^{-jkx} dx \ , \tag{3.4}$$

where $h(x)$ is the function in the spatial domain, $H(k)$ is the function in the wavenumber domain, x is distance, k is wavenumber, and j is the square root of -1. The left-hand side of equation (3.4) has units that are equal to the units of $h(x)$ multiplied by meters/radian. The limits of equation (3.4) can be changed to reflect a finite length interval, which is written as

$$H(k) = \frac{1}{2\pi}\int_0^L h(x)e^{-jkx}dx \ , \tag{3.5}$$

where L is the length of the interval.

In cases involving multiple discrete sensors, it is not possible to sample $h(x)$ continuously on the aperture interval. It is possible, however, to transform the measurements from the spatial domain to the wavenumber domain by means of a discrete Fourier transform having the form (Bendat and Piersol, 1980; Bendat and Piersol, 1986)

$$H_i(k) = H(i\Delta_k) = \frac{\Delta_x}{2\pi}\sum_{n=0}^{N-1} h(x_n)e^{-j\left(\frac{2\pi in}{N}\right)} \ , \tag{3.6}$$

where $H_i(k)$ is the discrete wavenumber domain transform, $h(x_n)$ is the discrete spatial domain data at the nth sensor, Δ_x (= L/N) is the separation distance between discrete sensors (m), N is the total number of sensors, i is a counter that runs from 1 to N, and Δ_k is the discrete wavenumber spacing of the transformed data (radians/meter). The wavenumber spacing is related to the aperture length, the spacing of the sensors, and the number of sensors by

$$\Delta_k = \frac{2\pi}{L} = \frac{2\pi}{N\Delta_x} \ . \tag{3.7}$$

Equation (3.6) provides a means to transform data sampled with multiple sensors into the wavenumber domain.

A process known as zero padding can be used to interpolate the data in wavenumber. This process involves using an additional M spatial data points in equation (3.6), all of which are set equal to zero. This approach results in a high accuracy interpolation between points in wavenumber using the discrete Fourier transform. The data are transformed into the wavenumber domain using the equations

$$H_i(k,\omega_0) = H(i\Delta_k) = \frac{\Delta_x}{2\pi} \sum_{n=0}^{N+M-1} w(x_n) h(x_n,\omega_0) e^{-j\left(\frac{2\pi i n}{N+M}\right)} \tag{3.8a}$$

and

$$\Delta_k = \left(\frac{N}{M+N}\right)\frac{2\pi}{L} = \frac{2\pi}{(M+N)\Delta_x} \ , \tag{3.8b}$$

where $w(x_n)$ is the spatial weighting function (window) of the discrete Fourier transform evaluated at position x_n and ω_0 represents a fixed frequency. Changing the window function allows data to be processed with different sidelobe levels and different mainlobe widths. The weighting function was normalized such that

$$\sum_{n=0}^{N+M-1} w(x_n) = 1 \ . \tag{3.9}$$

3.5. FREQUENCY-WAVENUMBER DOMAIN MEASUREMENTS

The discrete Fourier transform described previously was applied to the spatial domain measurements. Two aperture sizes were processed: one with n = 15 channels and a separation distance Δ_x of 0.00635 m (0.25 inch) and another with 8 channels and a separation distance of 0.0127 m (0.50 inch). Figures 3.8 to 3.27 illustrate the wavenumber cuts of the transformed spatial domain data starting at 100 Hz and ending at 480 Hz in 20-Hz increments. These data are displayed as a function of wavenumber using a uniform (rectangular) window with each individual weighting function equal to 0.005 (= $1/(N+M)$) and a zero pad of 185 (zeros) to 15 (actual data points) for the 15-channel aperture and a zero pad of 192 to 8 for the 8-channel aperture ($N+M$ = 200). The wave energy and wave speeds are identified on the plots. The wave speeds were determined using the equation

$$c = \frac{\omega}{k} \ , \tag{3.10}$$

where c is the apparent wave speed (m/s) sensed by the array, a term also frequently referred to as the phase velocity. Figure 3.28 is a plot of the theoretical shear wave speed of Hexcel 195-RE urethane and the measured apparent wave speeds of the array versus frequency. The theoretical shear wave speed was determined using (Verburg, 1983)

$$c_s = \sqrt{\frac{G}{\rho}} \ , \tag{3.11}$$

where c_s is the shear wave speed, G is the shear modulus, and ρ is the density. The area where the theoretical wave speed is decreasing with respect to frequency is shown (dashed line) because this is inconsistent behavior for the material according to many material laws. Note, however, that the measured shear wave speed is decreasing (with respect to frequency) near the frequencies where the material measurements predict a decreasing shear wave speed. Figure 3.29 shows the wavenumber-frequency surface of the measurements.

From figure 3.1, it is observed that turbulent flow induces a maximum spectrum level in the 100- to 125-Hz region. An examination of figures 3.2, 3.3, and 3.4 indicates that there is a relative minimum in the amplitude transfer function between the reference sensor and the locations at 1.09, 2.75, and 4.50 inches. A likely cause of these local minima in the transfer function is coherent destructive interference between different propagation modes (paths).

Consider the case of two coherent modes contributing to the waveform, $f_n(t)$, observed at the nth sensor location. This waveform can be expressed as

$$x_n(t) = \alpha_{n1} f(t - \tau_{n1}) + \alpha_{n2} f(t - \tau_{n2}) + v_n(t) \ , \tag{3.12}$$

where $f(t)$ is the source waveform at sensor 1, τ_{n1} is the effective propagation time relative to sensor 1 from the source to the nth sensor supported by the first propagation mode (path), and τ_{n2} is the effective propagation time relative to sensor 1 from the source to the nth sensor supported by the second mode (path). The parameter α_{np} is the relative attenuation of amplitude for the pth mode relative to the first mode referenced to the nth sensor. The waveform $v_n(t)$ is the additive noise at the nth sensor. Equation (3.12) has the Fourier transform

$$X_n(\omega) = F(\omega)e^{-j\omega\tau_{n1}}\left[\alpha_{n1} + \alpha_{n2}e^{-j\omega\Delta_{n,12}}\right] + V_n(\omega) \ , \tag{3.13}$$

where $F(\omega)$ is the Fourier transform of $f(t)$ and $\Delta_{n,12} = \tau_{n1} - \tau_{n2}$. The APSD for the nth sensor is

$$R_{nn}(\omega) = \overline{|X_n(\omega)|^2} \tag{3.14a}$$

or

$$R_{nn}(\omega) = \overline{|F(\omega)|^2}\left(\alpha_{n1}^2 + \alpha_{n2}^2 + 2\alpha_{n1}\alpha_{n2}\cos\omega\Delta_{n,12}\right) + \overline{|V_n(\omega)|^2} \ . \tag{3.14b}$$

The transfer function from sensor 1 to sensor n is

$$H_{1n}(\omega) = \frac{\overline{X_1(\omega)X_n^*(\omega)}}{R_{11}(\omega)} \ , \tag{3.15a}$$

which is also

$$H_{1n}(\omega) = \frac{\left[\alpha_{n1} + \alpha_{n2}e^{j\omega\Delta_{n,12}}\right]e^{-j\omega(\tau_{11}-\tau_{n1})}}{\left[\alpha_{11} + \alpha_{12}e^{j\omega\Delta_{1,12}}\right] + \left(\dfrac{\overline{|V_1(\omega)|^2}}{\overline{|F(\omega)|^2}}\right)\left[\alpha_{11} + \alpha_{12}e^{-j\omega\Delta_{1,12}}\right]^{-1}} \ , \tag{3.15b}$$

where $\overline{|F(\omega)|^2}\big/\overline{|V_1(\omega)|^2}$ is the SNR at frequency ω (rad/s). At high SNR, equation (3.15b) gives the squared amplitude of the transfer function as

$$|H_{1n}(\omega)|^2 = \left[\frac{\alpha_{n1}^2 + \alpha_{n2}^2 + 2\alpha_{n1}\alpha_{n2}\cos\omega\Delta_{n,12}}{\alpha_{11}^2 + \alpha_{12}^2 + 2\alpha_{11}\alpha_{12}\cos\omega\Delta_{1,12}}\right] , \tag{3.16}$$

and shows the linear dependence of phase with respect to frequency. It is argued that because sensor 1 is located on the urethane block surface at the point closest to the blockage, there is predominantly only a single path from the source to sensor 1, as shown in figure 3.30. Hence, $\tau_{11} = \tau_{12}$ and $\Delta_{1,12} = \tau_{11} - \tau_{12} = 0$. This argument is supported, at least above 60 Hz, by the fact that there are no nulls in the APSD of figure 3.1 that would indicate intermodal destructive interference. For sensor locations n = 2, 3, 4 . . . , equation (3.16) predicts a local minimum at $\omega_{\min}\Delta_{n,12} = (2k+1)\pi$. For a mean propagation velocity of c = 13 m/s, an effective propagation path length difference, $\delta_{n,12}$, between modes 1 and 2 is seen to be

$$\delta_{n,12}(k) = \frac{c(2k+1)}{2f_{\min}} . \tag{3.17}$$

From figure 3.3, with a sensor separation of 2.75 inches (6.99 cm), the local minimum in the transfer function at approximately 312 Hz predicts a $k = 0$ mode interference effective path length difference of

$$\delta_{n,12}(0) = 0.82 \text{ inch } (2.1 \text{ cm}) . \tag{3.18}$$

Similarly, for the weaker SNR null at 360 Hz in figure 3.4 (separation 4.5 inches (11.43 cm)), an effective path length difference of 0.75 inch (1.9 cm) is predicted. For the assumed two mode model, the effective path length differences calculated above for the two propagation modes are entirely consistent with the test geometry. That is, the effective path length differences are less than any direct path propagation distance. In fact, the calculated effective path differences are supportive of a model that includes a direct path and a second path, perhaps a surface wave, from the source to the sensors. However, a more exact understanding of the actual spatial extent of the turbulence-induced excitation source and the full solution of the frequency domain (Helmholtz) wave equation is clearly needed to substantiate the very basic approach taken above.

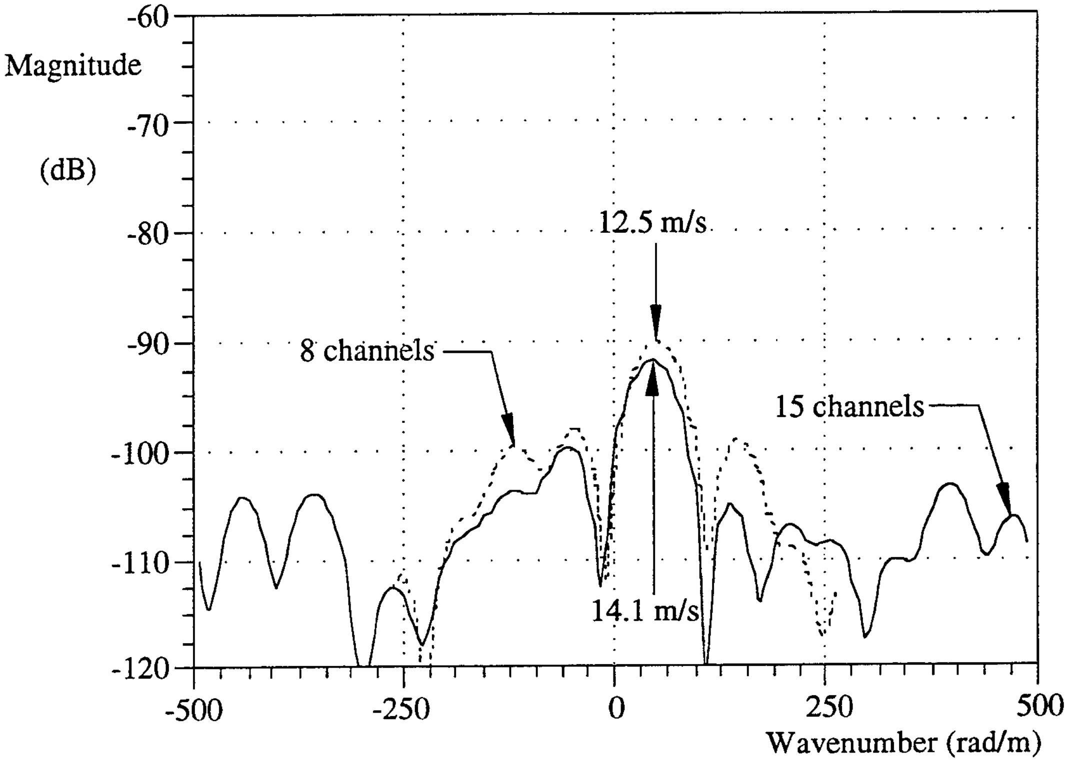

Figure 3.8. Wavenumber Cut at 100 Hertz

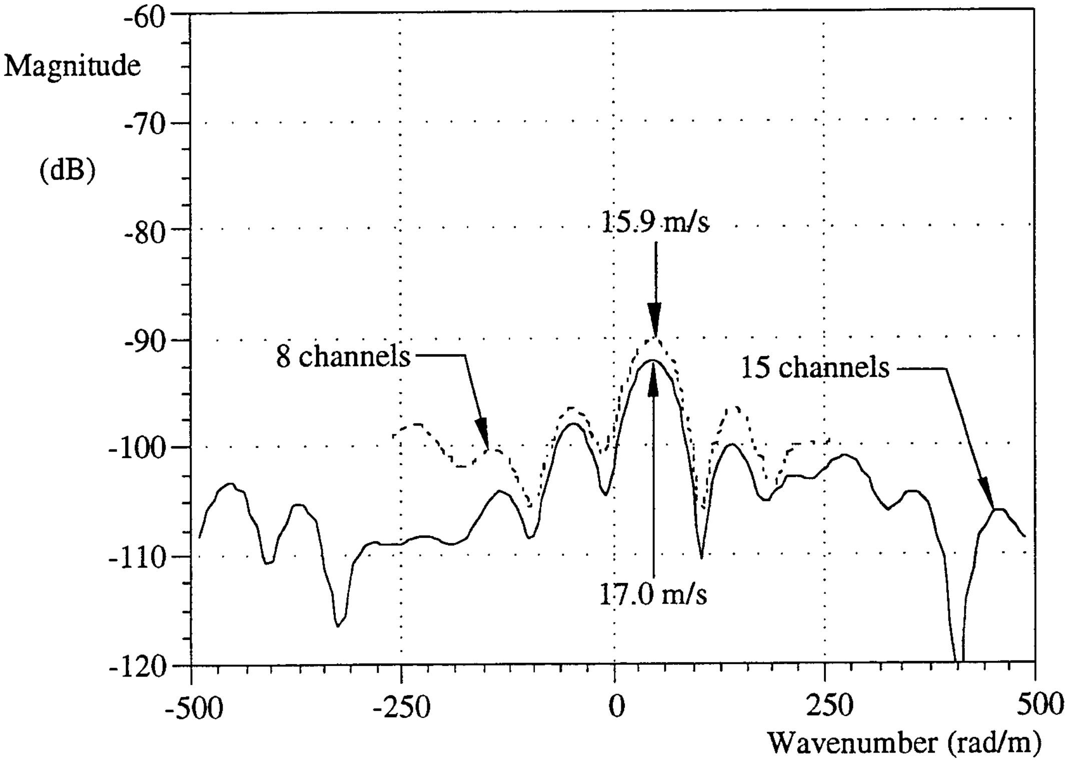

Figure 3.9. Wavenumber Cut at 120 Hertz

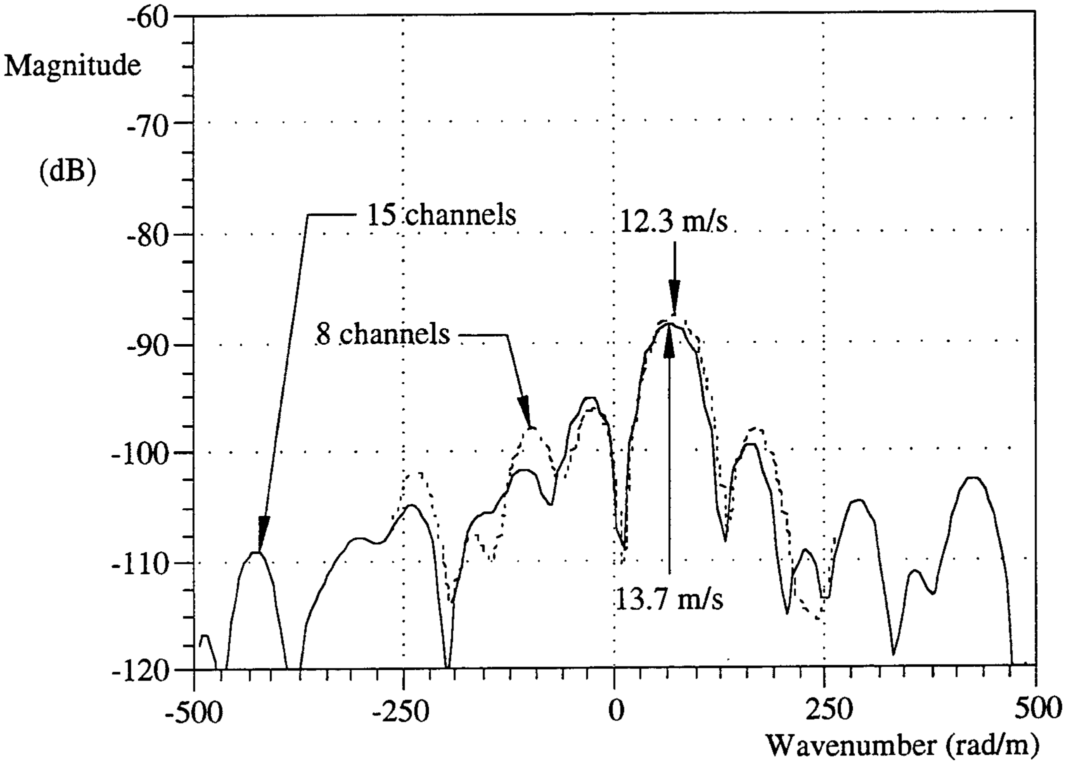

Figure 3.10. Wavenumber Cut at 140 Hertz

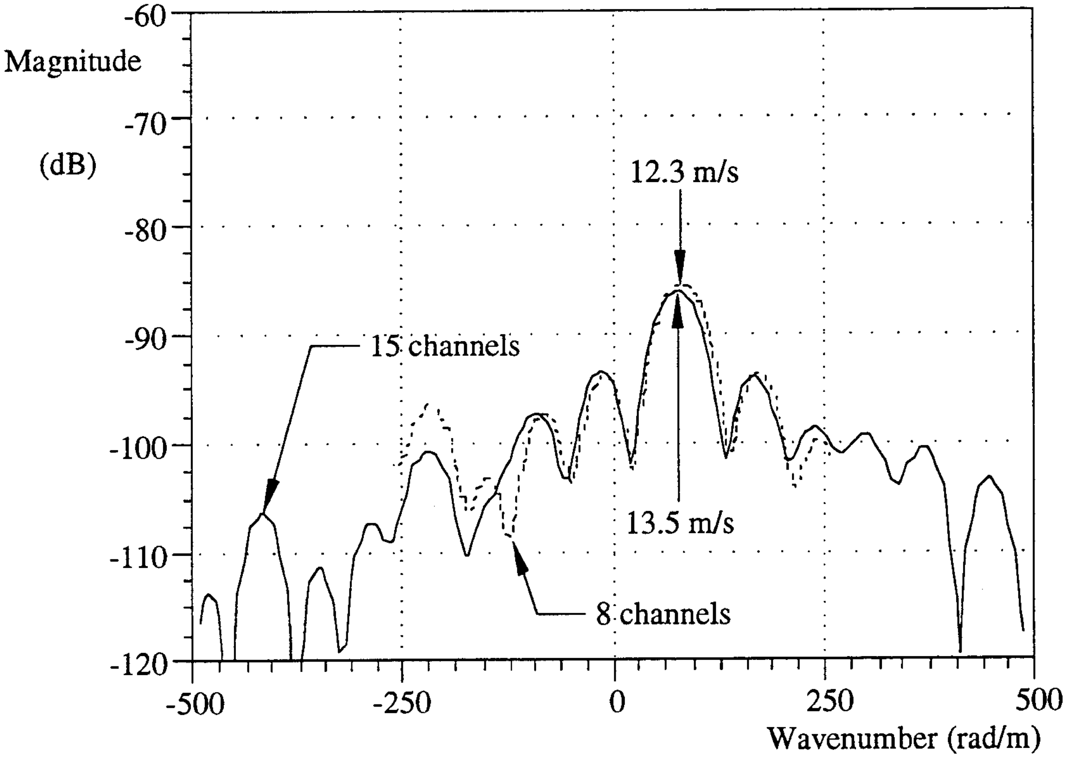

Figure 3.11. Wavenumber Cut at 160 Hertz

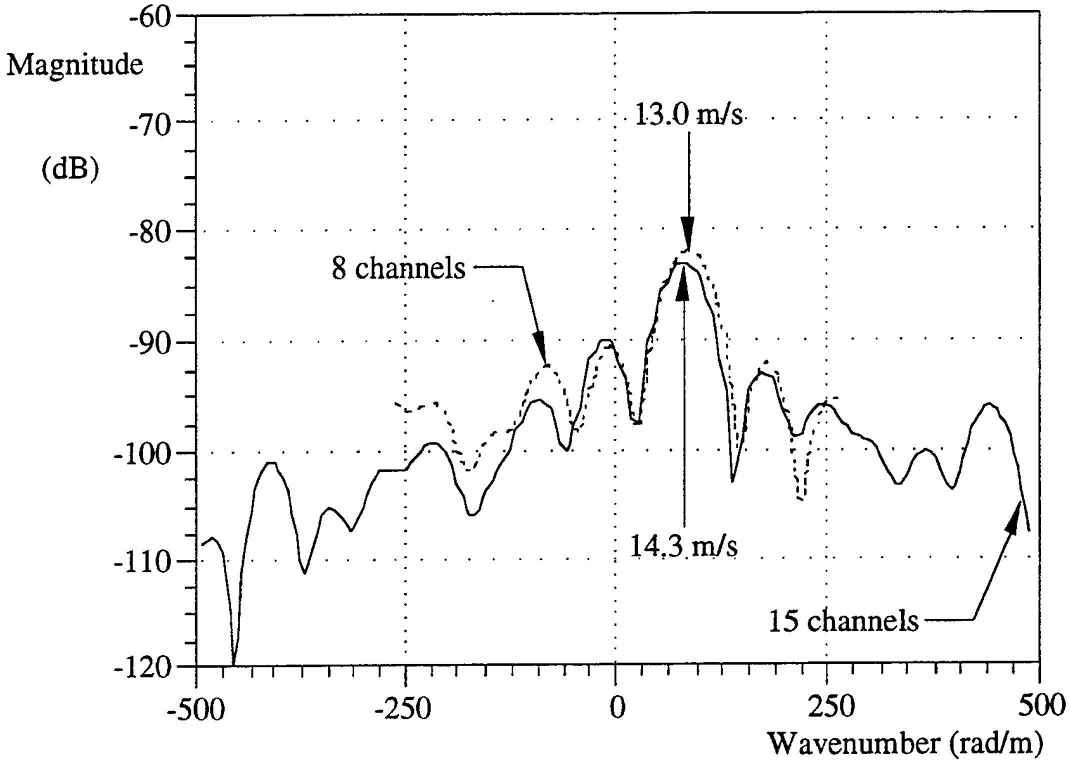

Figure 3.12. Wavenumber Cut at 180 Hertz

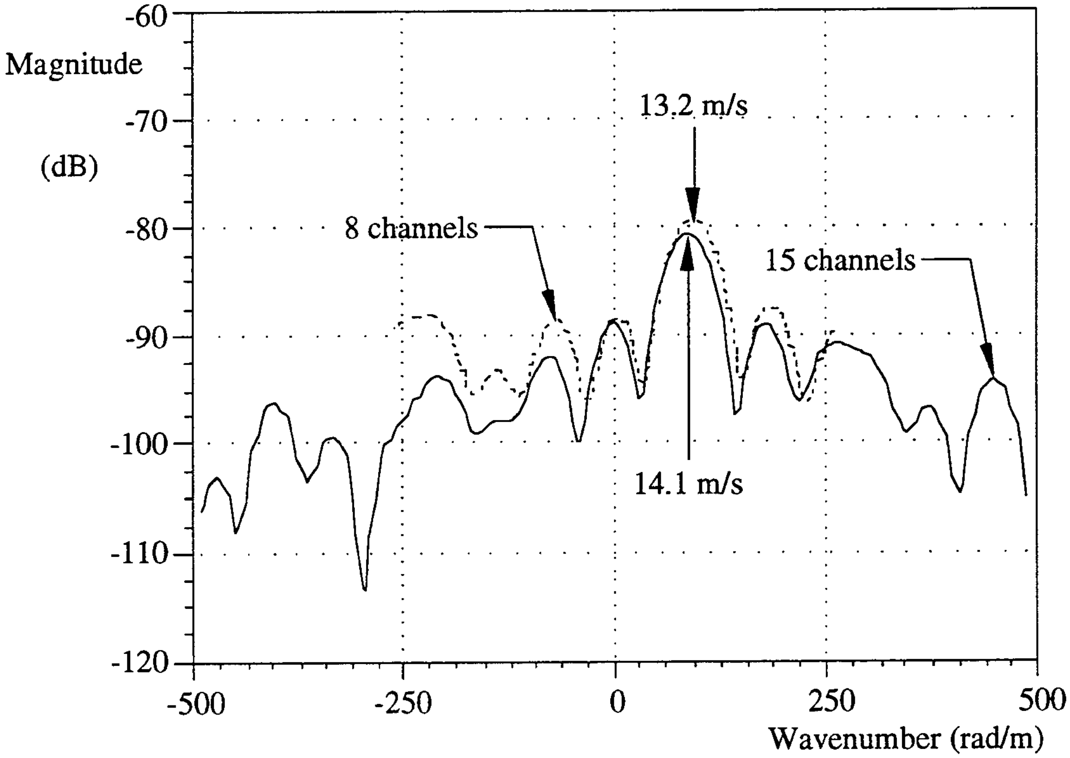

Figure 3.13. Wavenumber Cut at 200 Hertz

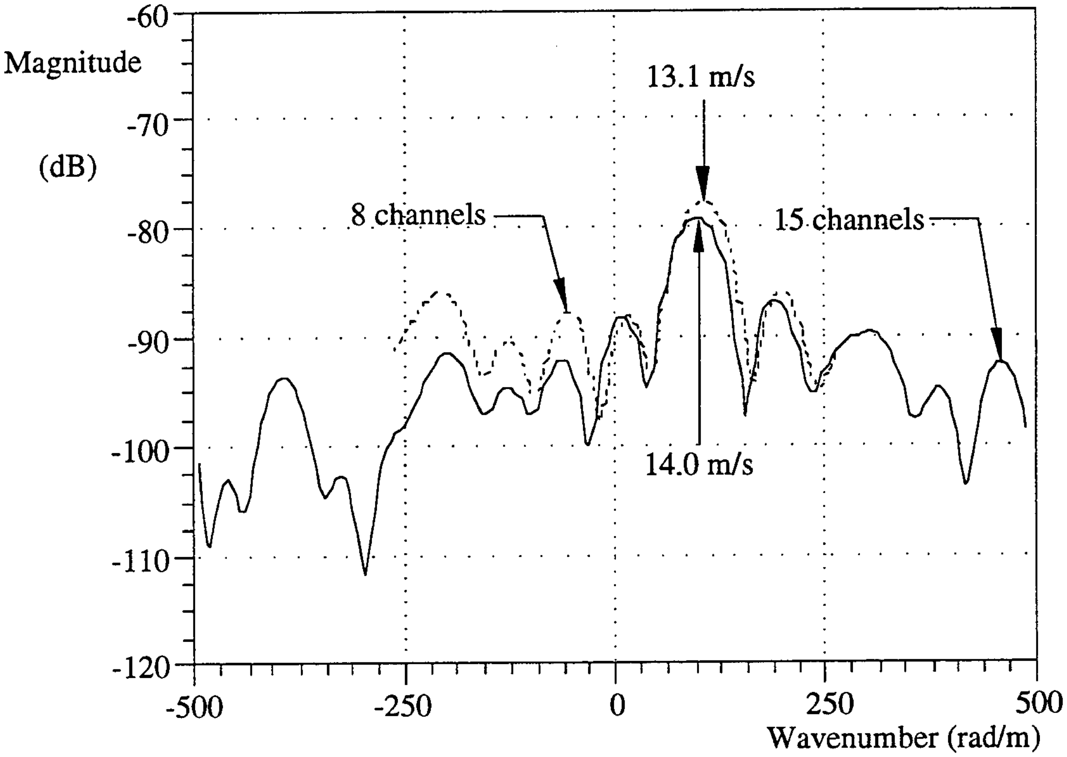

Figure 3.14. Wavenumber Cut at 220 Hertz

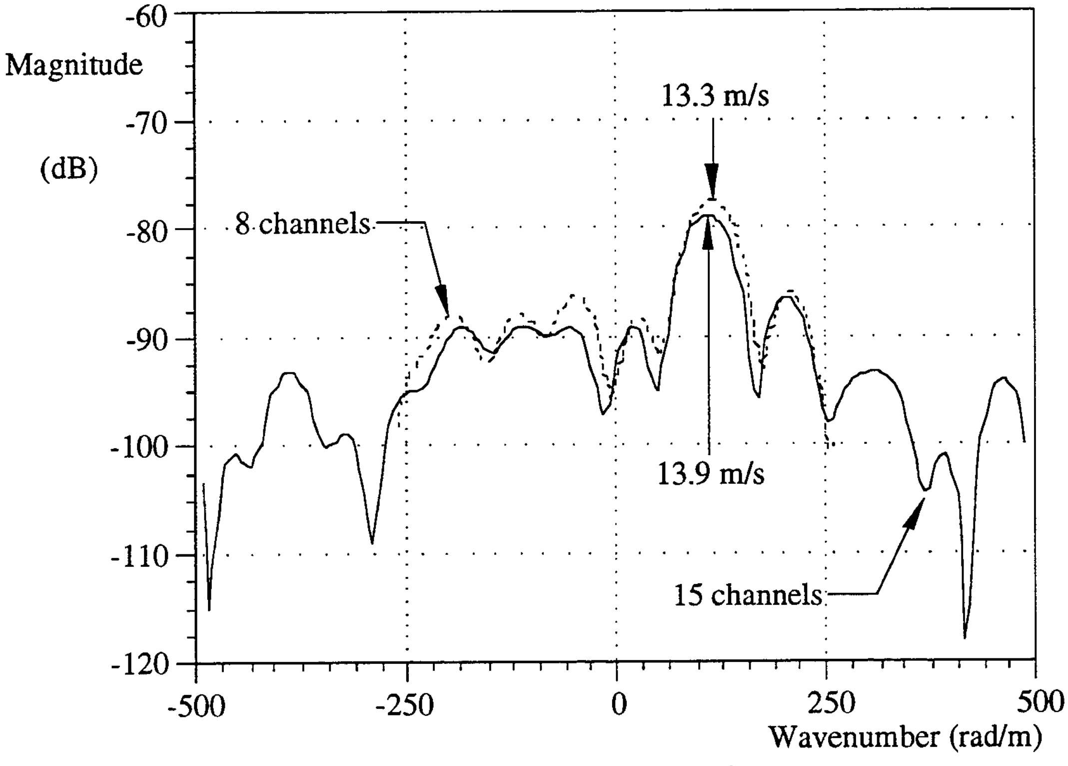

Figure 3.15. Wavenumber Cut at 240 Hertz

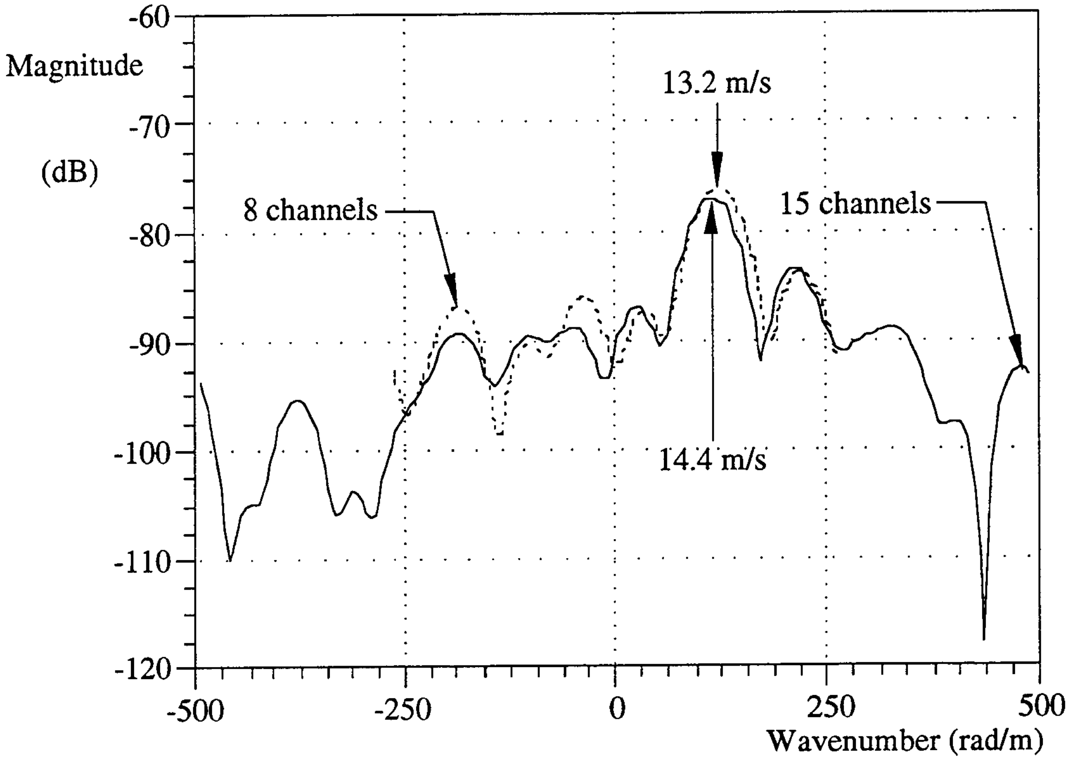

Figure 3.16. Wavenumber Cut at 260 Hertz

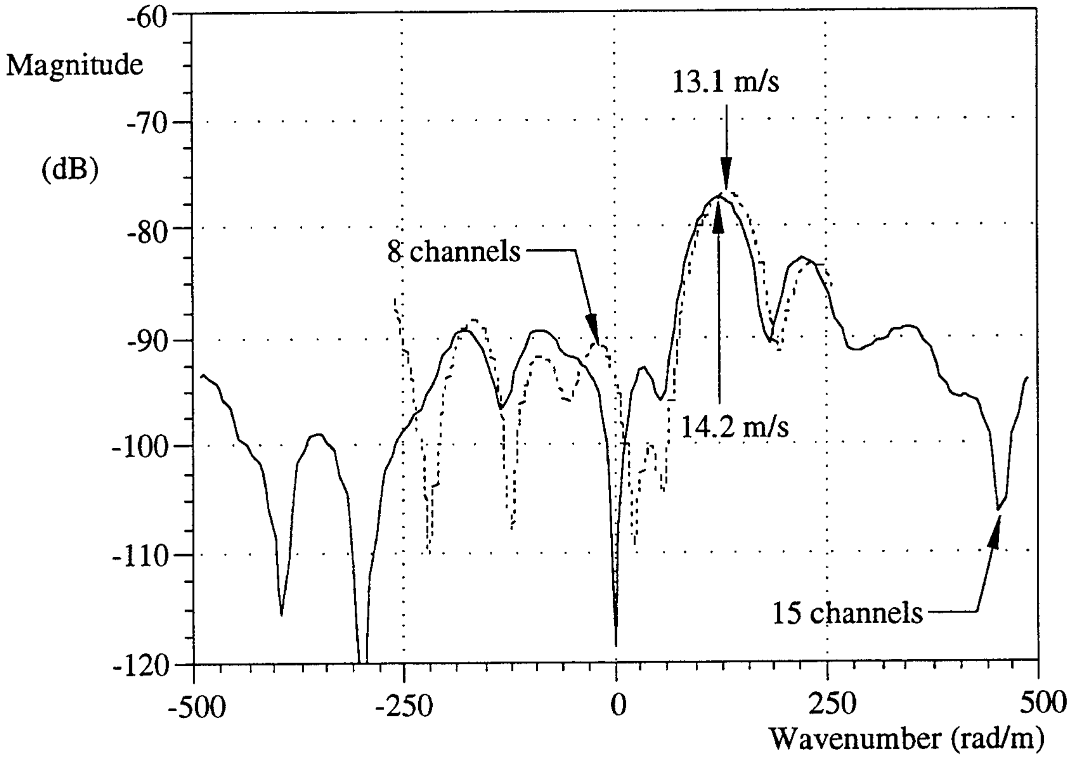

Figure 3.17. Wavenumber Cut at 280 Hertz

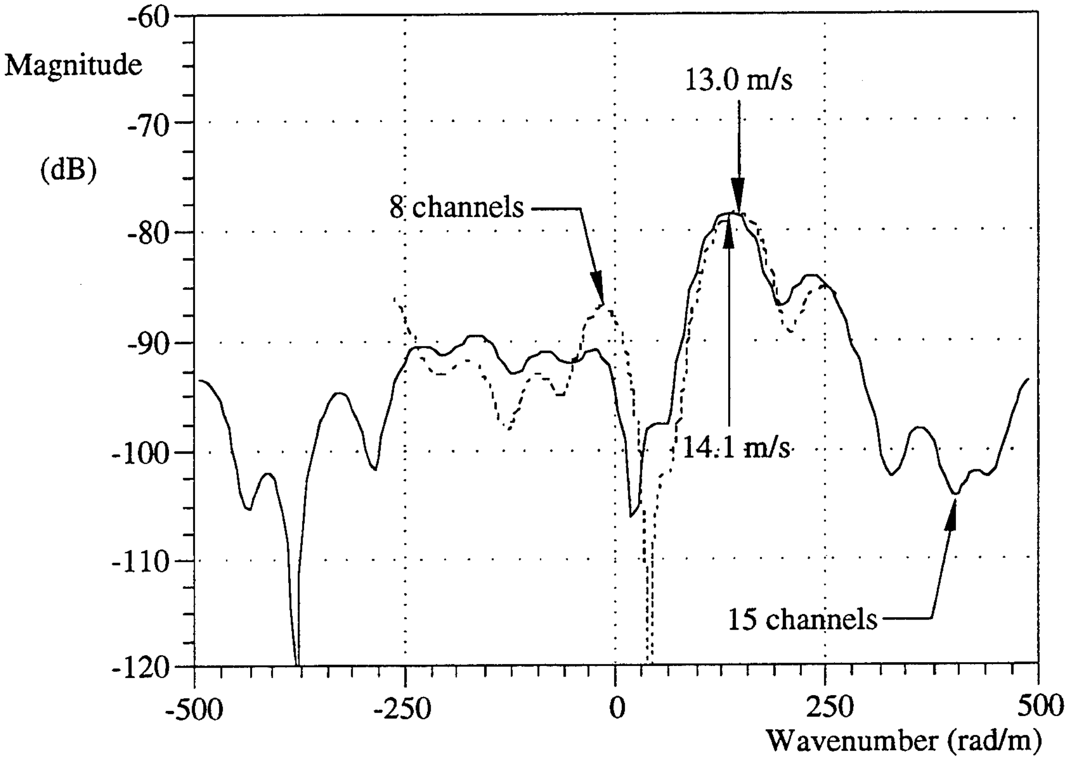

Figure 3.18. Wavenumber Cut at 300 Hertz

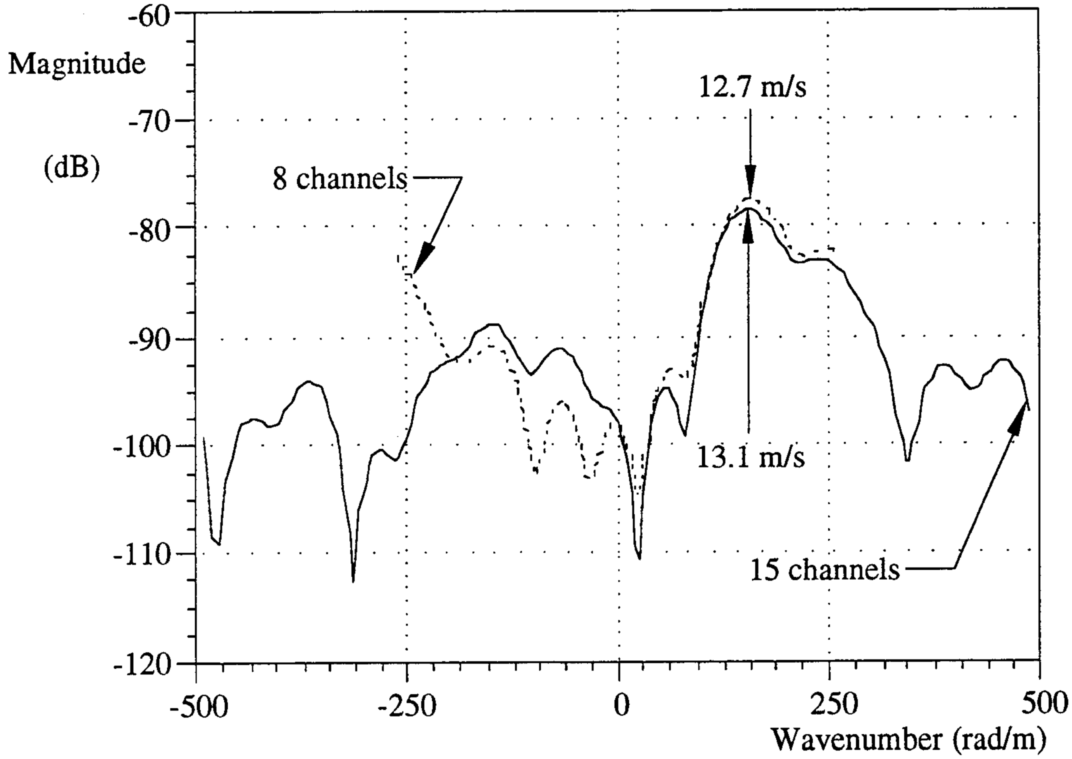

Figure 3.19. Wavenumber Cut at 320 Hertz

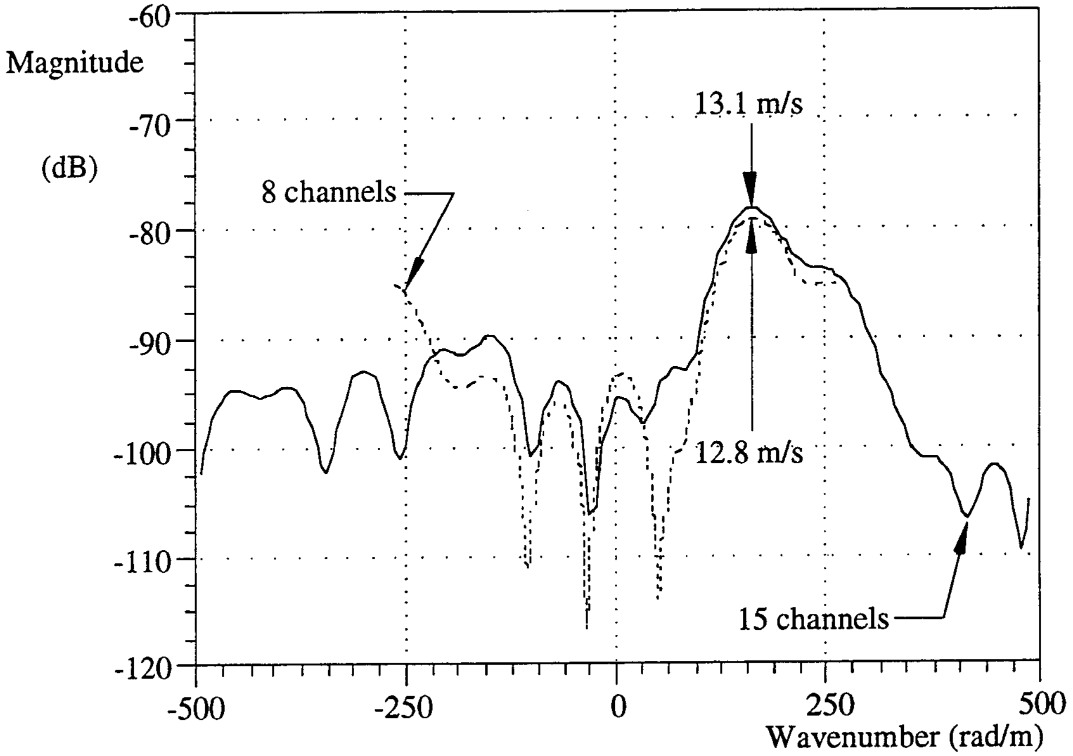

Figure 3.20. Wavenumber Cut at 340 Hertz

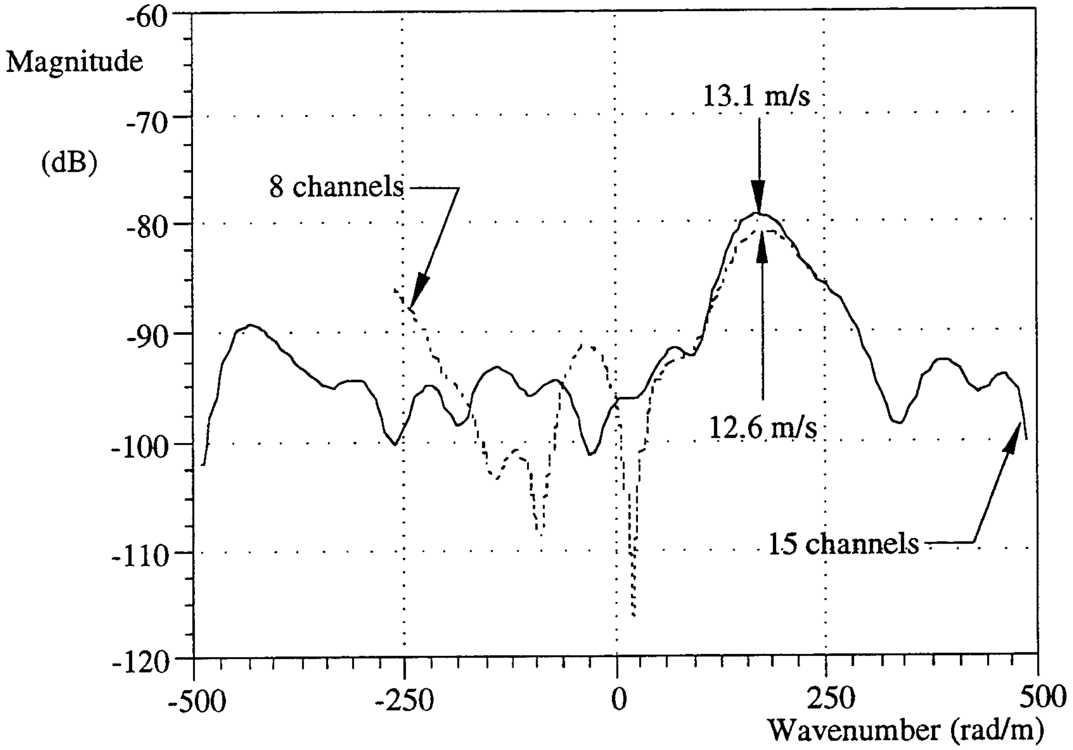

Figure 3.21. Wavenumber Cut at 360 Hertz

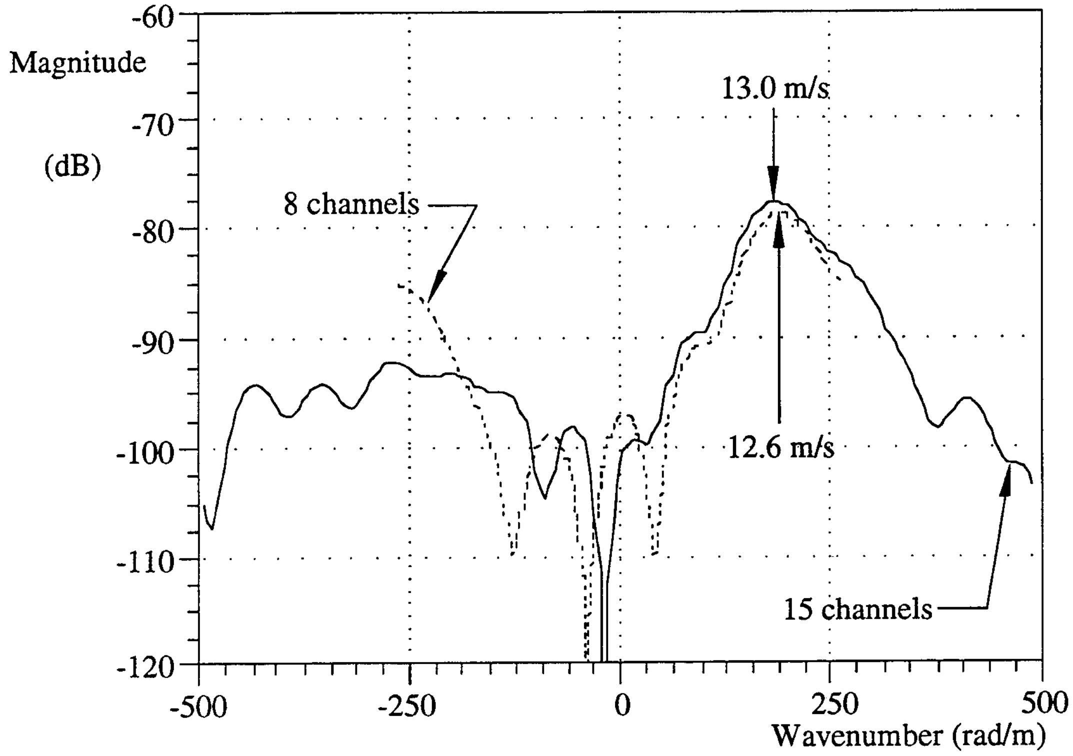

Figure 3.22. Wavenumber Cut at 380 Hertz

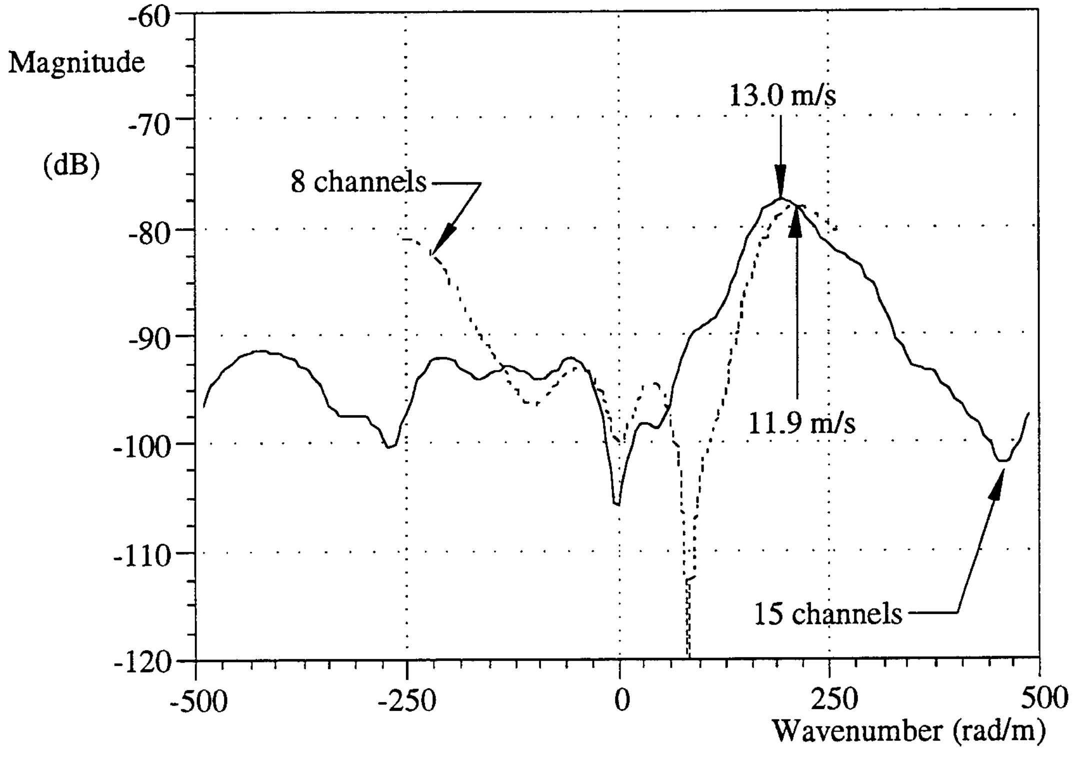

Figure 3.23. Wavenumber Cut at 400 Hertz

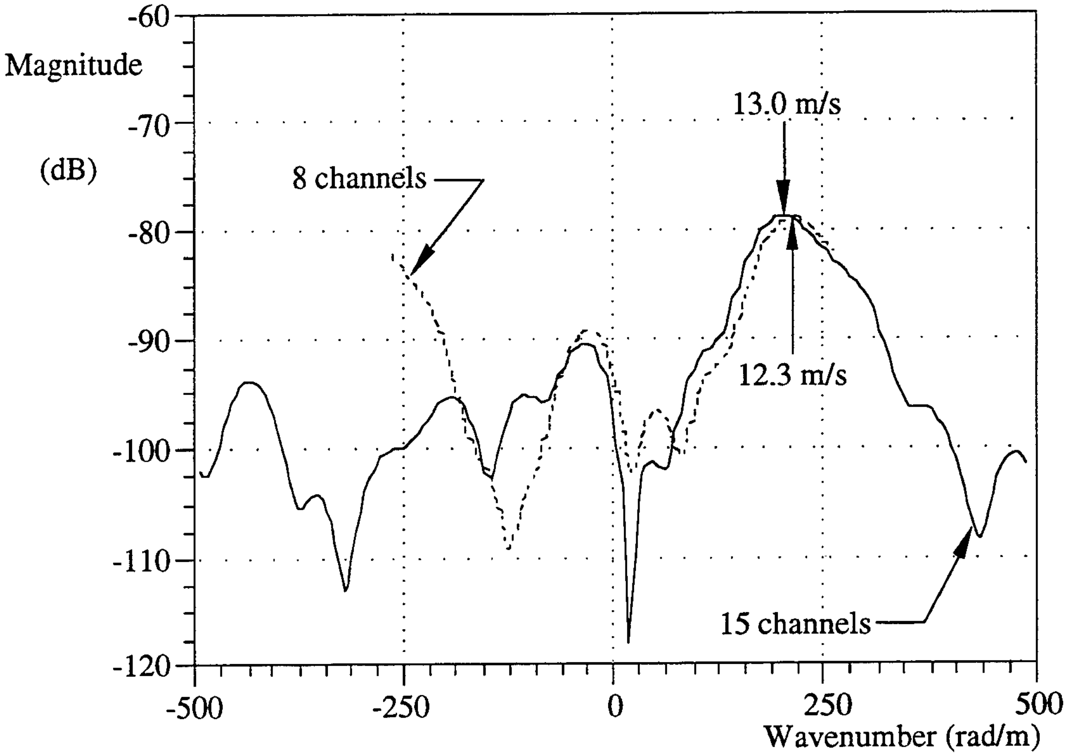

Figure 3.24. Wavenumber Cut at 420 Hertz

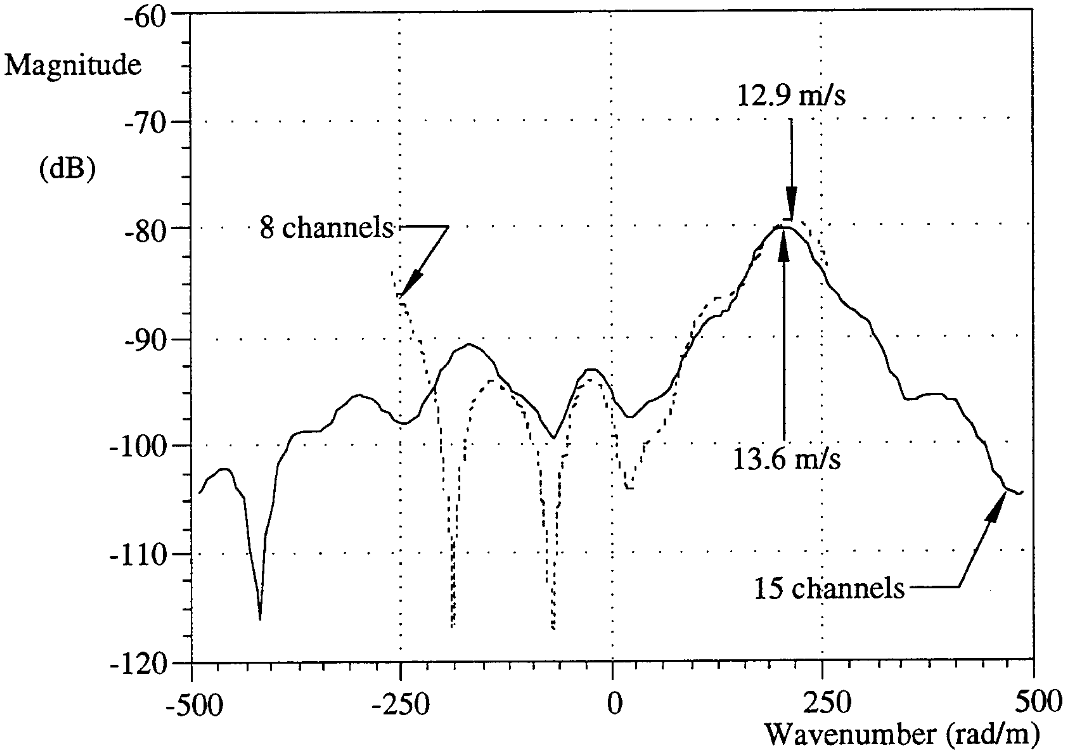

Figure 3.25. Wavenumber Cut at 440 Hertz

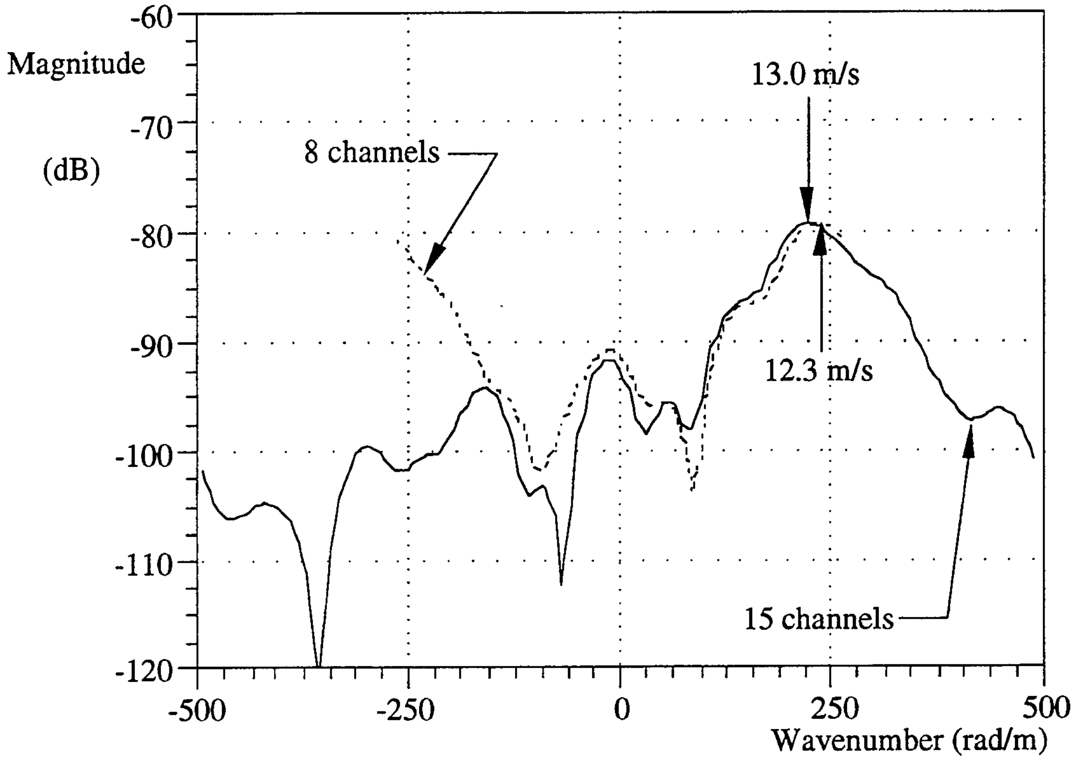

Figure 3.26. Wavenumber Cut at 460 Hertz

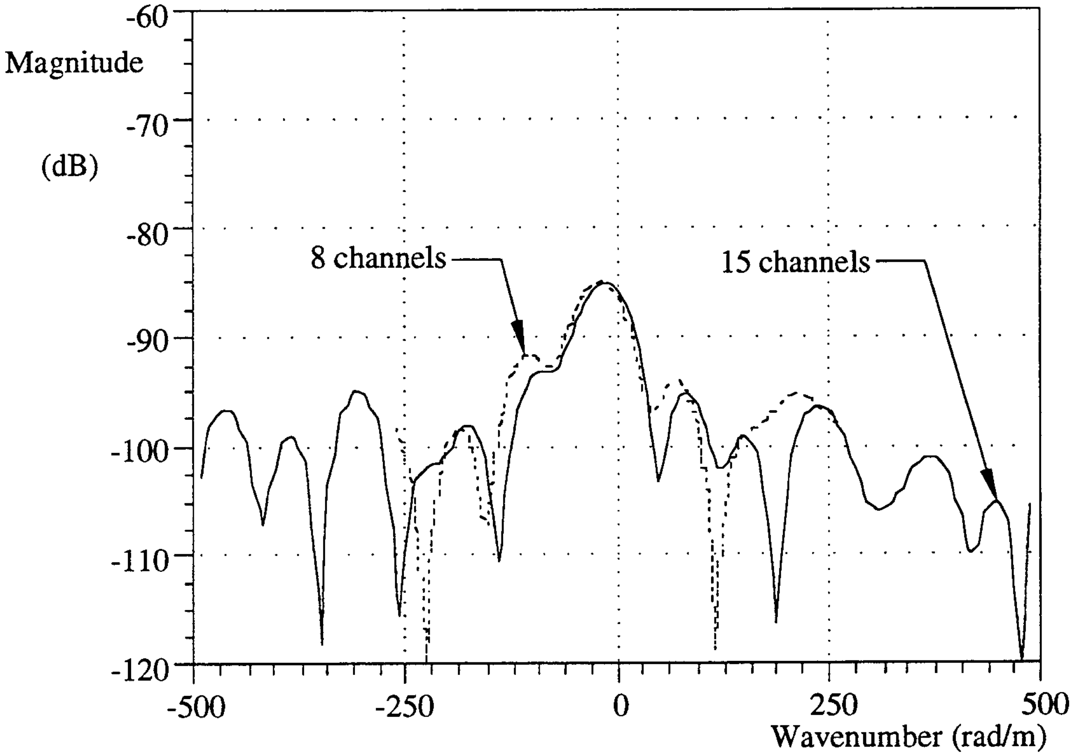

Figure 3.27. Wavenumber Cut at 480 Hertz

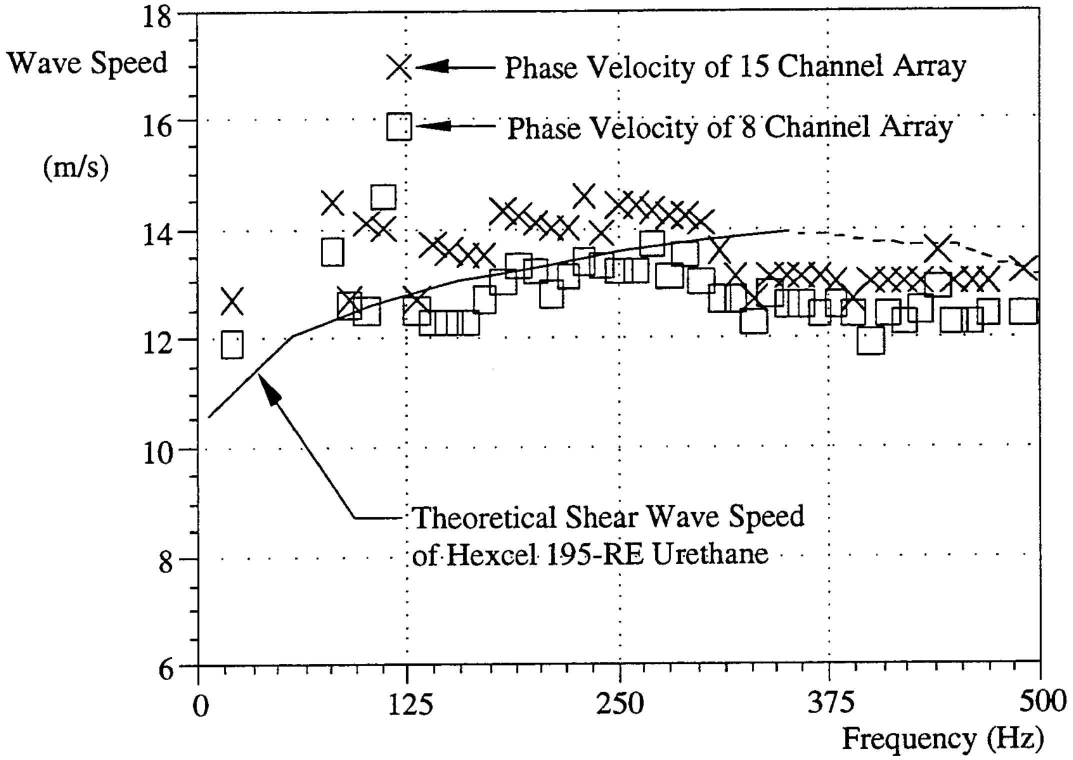

Figure 3.28. Comparison of Theoretical and Measured Wave Speeds

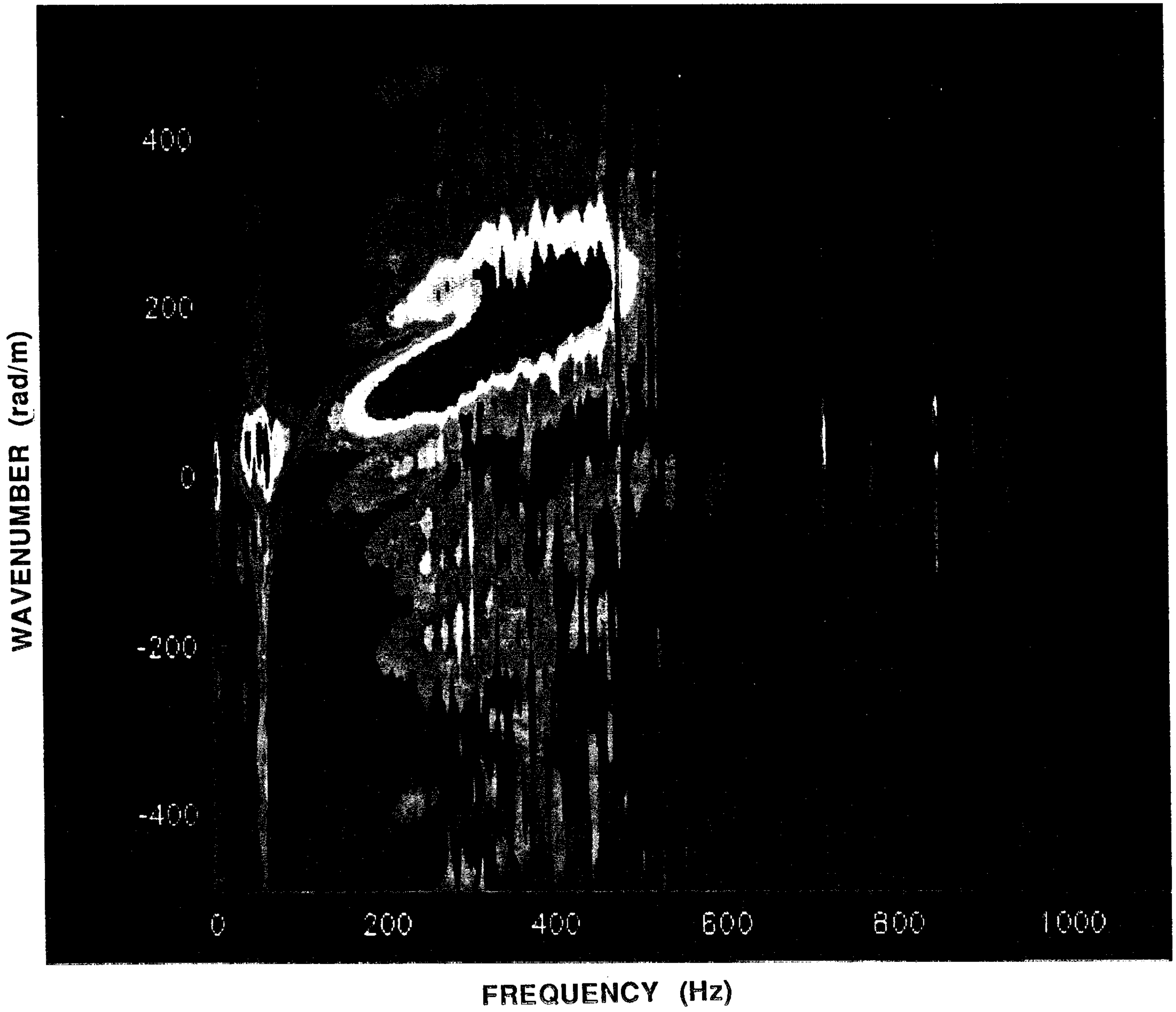

Figure 3.29. Wavenumber-Frequency Surface of Measured Data

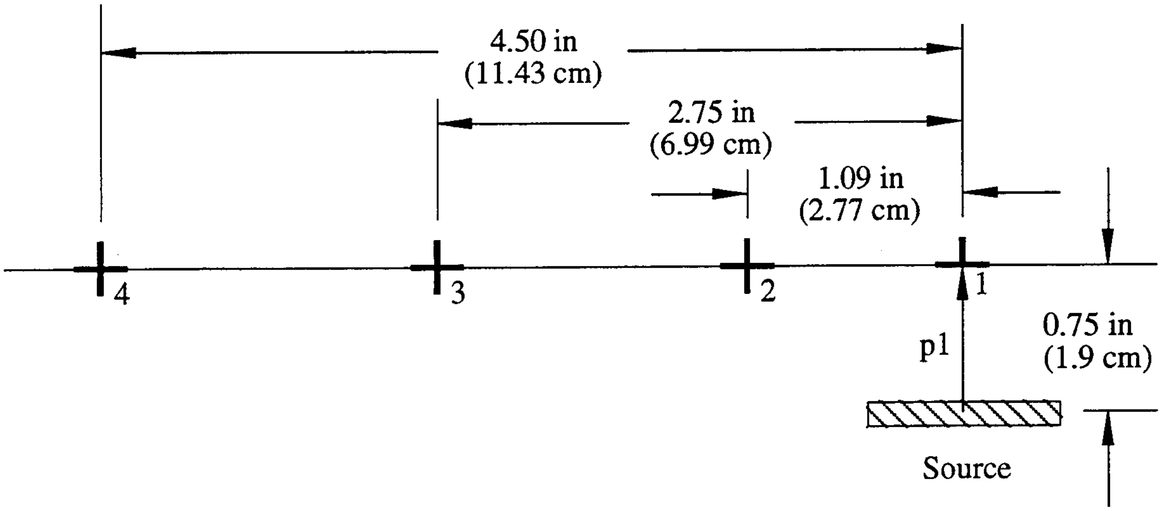

Figure 3.30. Geometry of Four Sensor Locations Used to Measure Transfer Functions Between Sensor Locations (1 to 2), (1 to 3), and (1 to 4). Energy Propagation From the Source to Sensor Location 1 is Assumed To Be Single Mode, Direct Path (p1).

3.6. SUMMARY

The propagating energy produced by the blockages in the tubing can be measured with sensors applied to the surface of the urethane solid. Transferring the data into the wavenumber domain provides a method to identify wave speeds of coherent energy in the solid block.

CHAPTER 4. PASSIVE IMAGING OF A SIMULATED EXTENDED NEARFIELD RADIATOR

4.1. INTRODUCTION

The array-source geometry for the simulation of an extended nearfield source is depicted in figure 4.1. The eight-sensor line array is located on the x-axis, and all dimensions are in centimeters. A radiating source is simulated using a total of 64 point sources distributed in the cylinder. The sources were equally spaced in each direction: radius, length of the cylinder, and circular cross section. Each point source signal and received sensor noise were simulated using independent normal Gaussian random numbers and a sampling rate of 2000 Hz. The received signal at each passive sensor is the sum of signals from each of the point sources and noise. Linear time delay interpolation and a wave speed of 10 m/s were used to calculate the delay from each source to each sensor. From the geometry, it is clear that the effective source is extended and nearfield. The received sensor signal was filtered using a Butterworth filter of order 14, with a bandpass from 100 to 350 Hz and a stopband from 50 to 400 Hz.

4.2. MUSIC AND MAGDR SIGNAL PROCESSING

Eigenvectors and eigenvalues of the sensor-to-sensor cross spectral density matrix (CSDM) were obtained using the MATLAB singular value decomposition (SVD) method. The eight-by-eight CSDM was estimated at 250 Hz by using a 256-point block fast Fourier transform (FFT) and a 40-snapshot (5.12 sec) average. A Hamming window was applied to the input sample time data before the FFT transform. The eigenvalue amplitudes for sensor output SNR ratios of 12 and 3 dB are plotted in figures 4.2 and 4.3, respectively. The maximum array gain distortionless (MAGDR) beamformer and MUSIC direction finder (DF) responses were calculated for SNR levels of 12 and 3 dB. For the MUSIC response, the eigenvectors corresponding to the three dominant eigenvalues were used as the source vector subspace. The MAGDR beamformer and

MUSIC DF normalized response images, viewed at a vertical angle of 30 degrees, are presented in figures 4.4-4.15 with a spatial resolution of 0.25 cm in each dimension.

Figures 4.4, 4.8, and 4.12 are the MUSIC DF response functions in the x-y, y-z, and x-z planes, respectively, for a sensor output SNR of 12 dB. Figures 4.5, 4.9, and 4.13 are the MAGDR beamformer response functions in the x-y, y-z, and x-z planes, respectively, for a sensor output SNR of 12 dB. Figures 4.6, 4.10, and 4.14 are the MUSIC DF response functions in the x-y, y-z, and x-z planes, respectively, for a sensor output SNR of 3 dB. Figures 4.7, 4.11, and 4.15 are the MAGDR beamformer response functions in the x-y, y-z, and x-z planes, respectively, for a sensor output SNR of 3 dB. All the response planar cuts were chosen to intersect the source volume.

The following conclusions can be drawn from the response plots:

- The largest eigenvalue becomes less dominant as the sensor output SNR decreases.
- A cusp of ambiguity for response plots in the x-z plane occurs because of the conical response pattern for the linear sensor array.
- The y-z response plot has some feature in the z-direction due to the nearfield. This perspective is the most informative because it gives the best indicator of distance (2 cm) to the source for z = 0 and allows an approximation of 10 log 8 = 9 dB for the SNR improvement due to beamforming (see figure 4.12).
- For the 3-dB SNR case, the spatial response results in high sidelobes and ambiguity (compare figure 4.14 to figure 4.12).

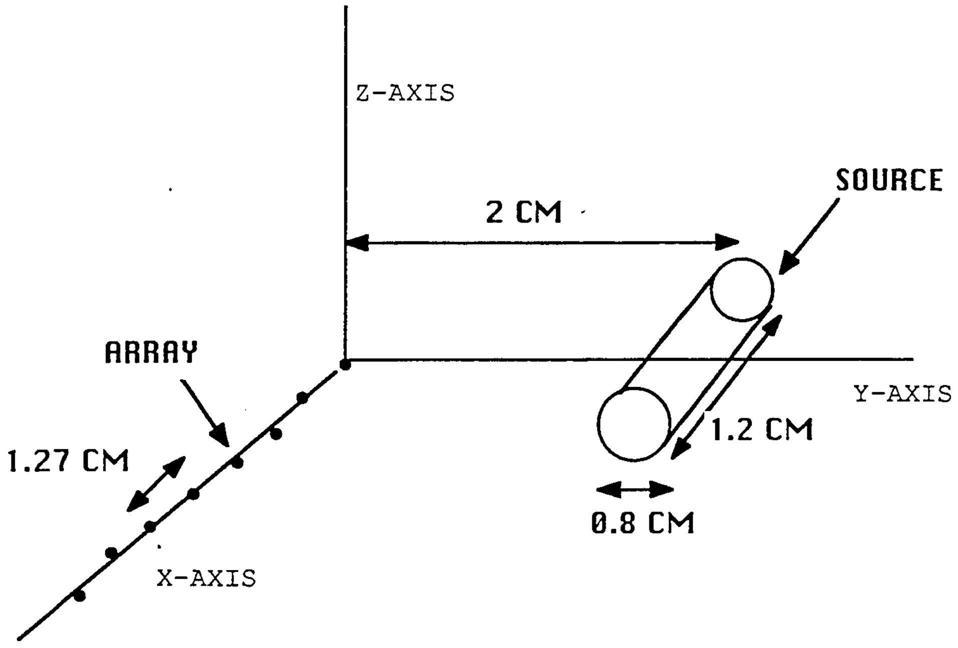

Figure 4.1. Array and Source Geometry

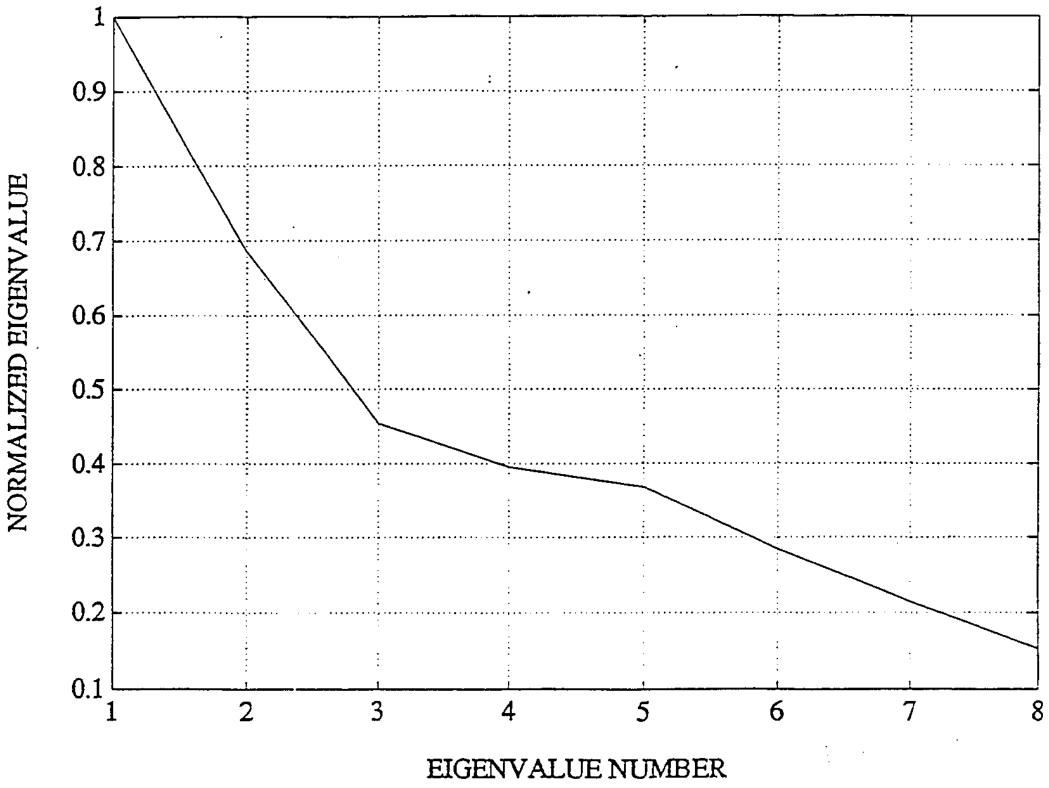

Figure 4.2. Amplitude of Eight-Sensor Linear Array CSDM Eigenvalues for a Sensor Output SNR of 12 dB at 250 Hz

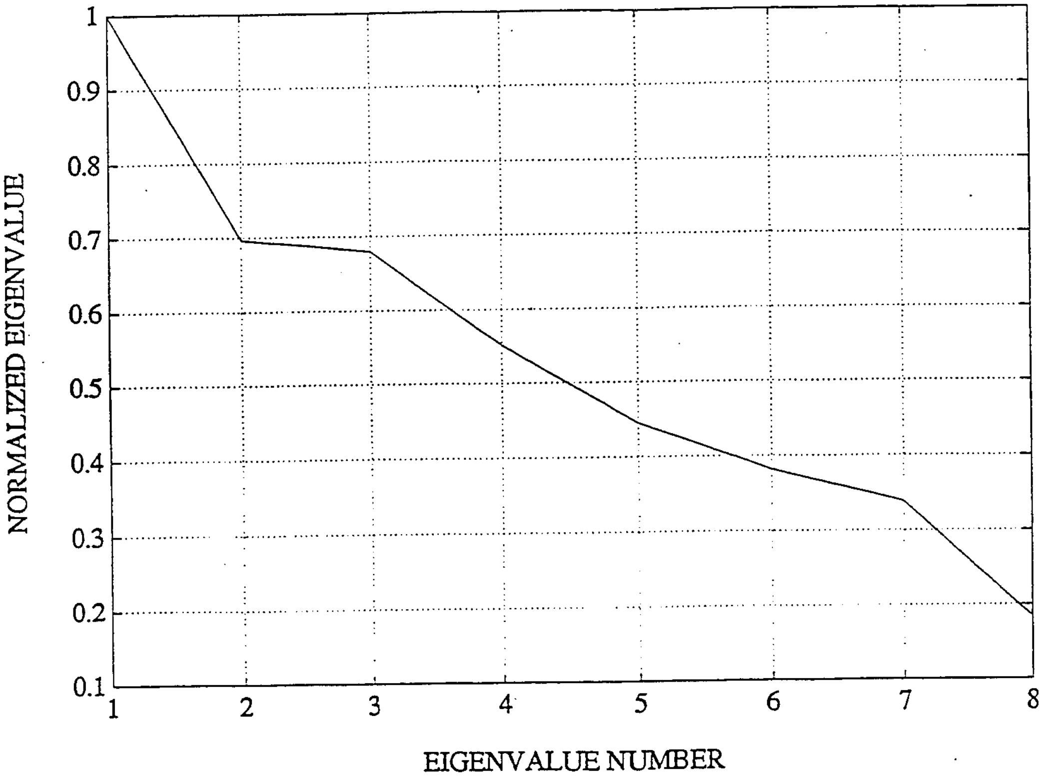

Figure 4.3. Amplitude of Eight-Sensor Linear Array CSDM Eigenvalues for a Sensor Output SNR of 3 dB at 250 Hz

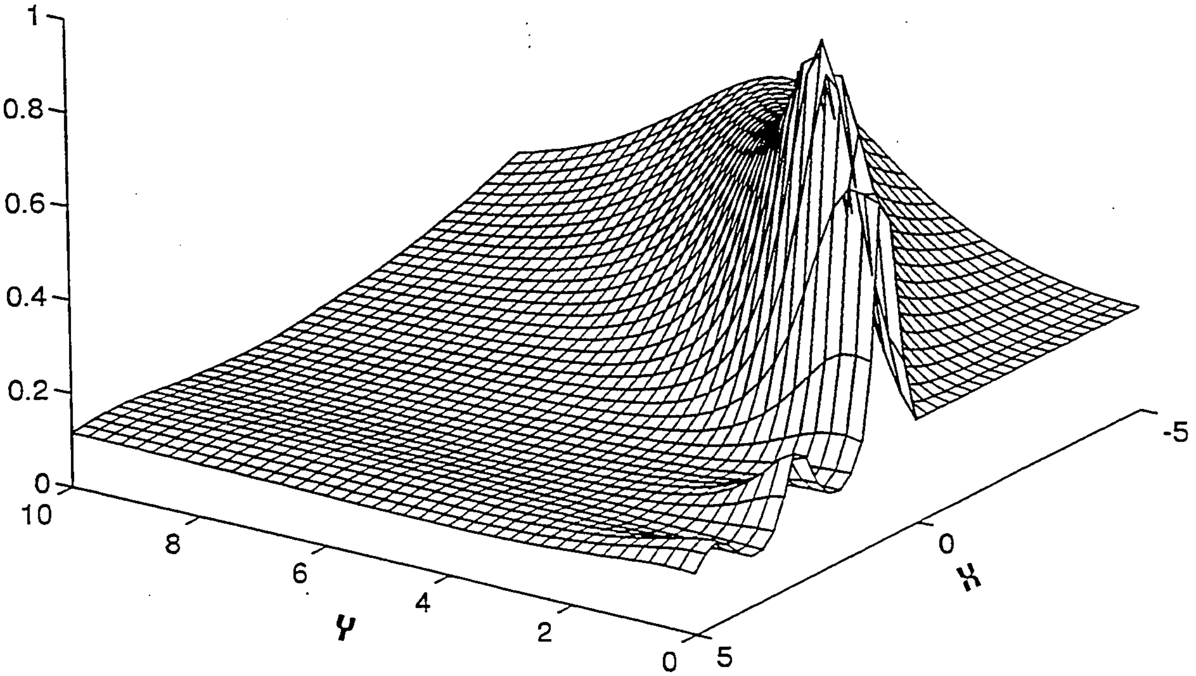

Figure 4.4. Normalized MUSIC Response in the x-y Plane for a Sensor Output SNR of 12 dB at 250 Hz. Maximum and Minimum Response Values Are 1.0 (x = 0.25, y = 1.25) and 0.103 (x = 1.25, y = 10.0)

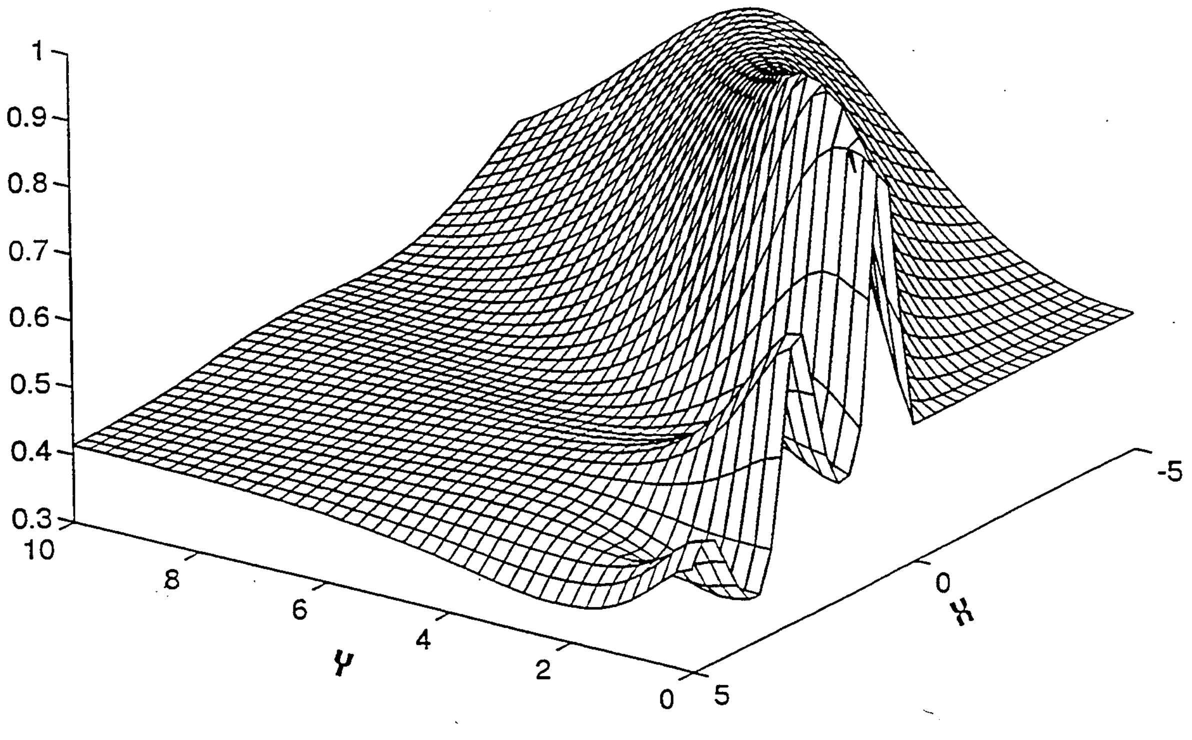

Figure 4.5. Normalized MAGDR Response in the x-y Plane for a Sensor Output SNR of 12 dB at 250 Hz. Maximum and Minimum Response Values Are 1.0 (x = 0.25, y = 1.5) and 0.3536 (x = 5.0, y = 2.25)

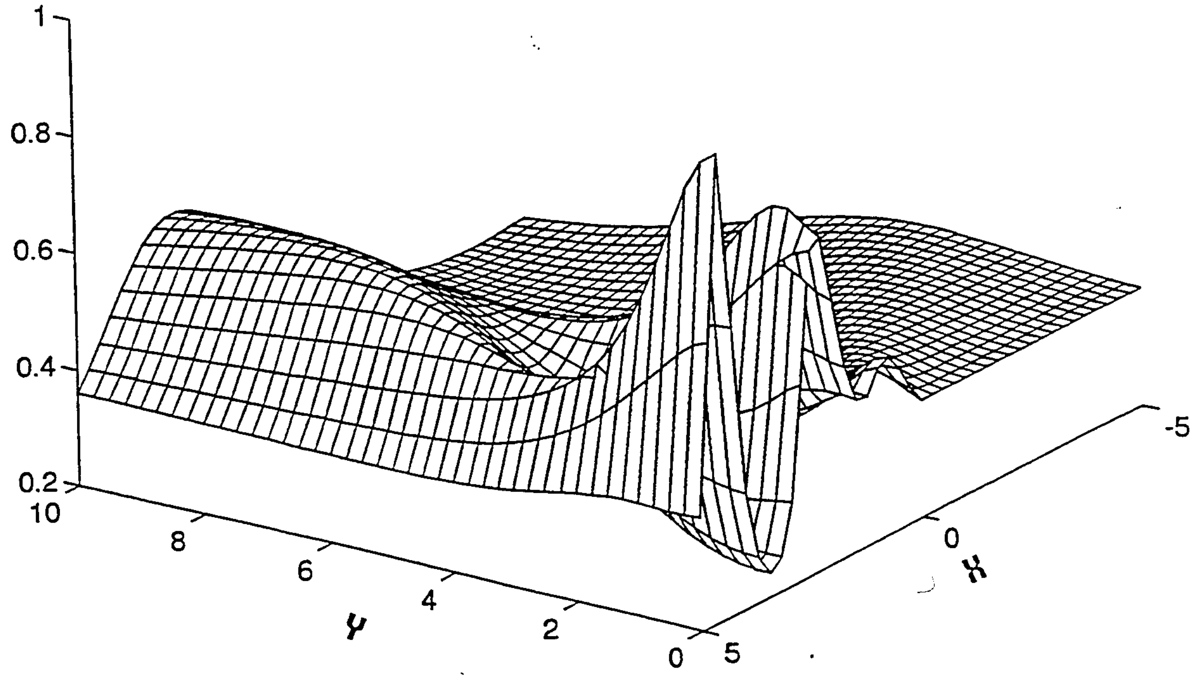

Figure 4.6. Normalized MUSIC Response in the x-y Plane for a Sensor Output SNR of 3 dB at 250 Hz. Maximum and Minimum Response Values Are 1.0 (x = 4.5, y = 0.0) and 0.2395 (x = 3.5, y = 0.0)

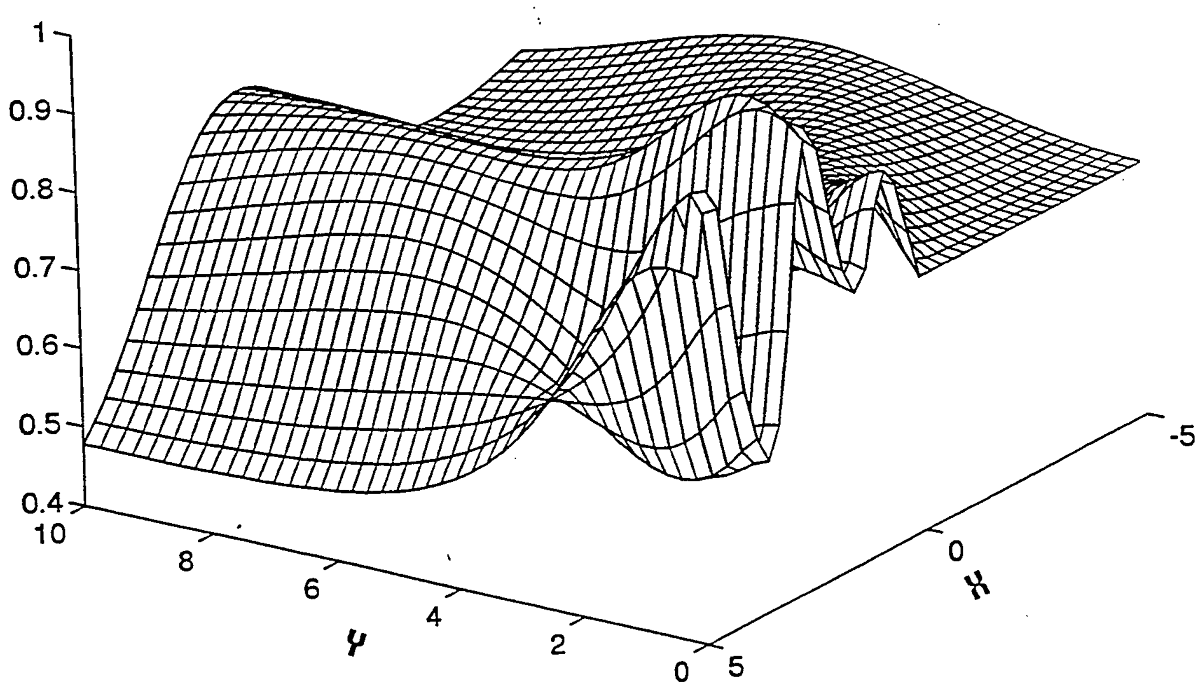

Figure 4.7. Normalized MAGDR Response in the x-y Plane for a Sensor Output SNR of 3 dB at 250 Hz. Maximum and Minimum Response Values Are 1.0 (x = 2.25, y = 1.0) and 0.477 (x = 5.0, y = 9.0)

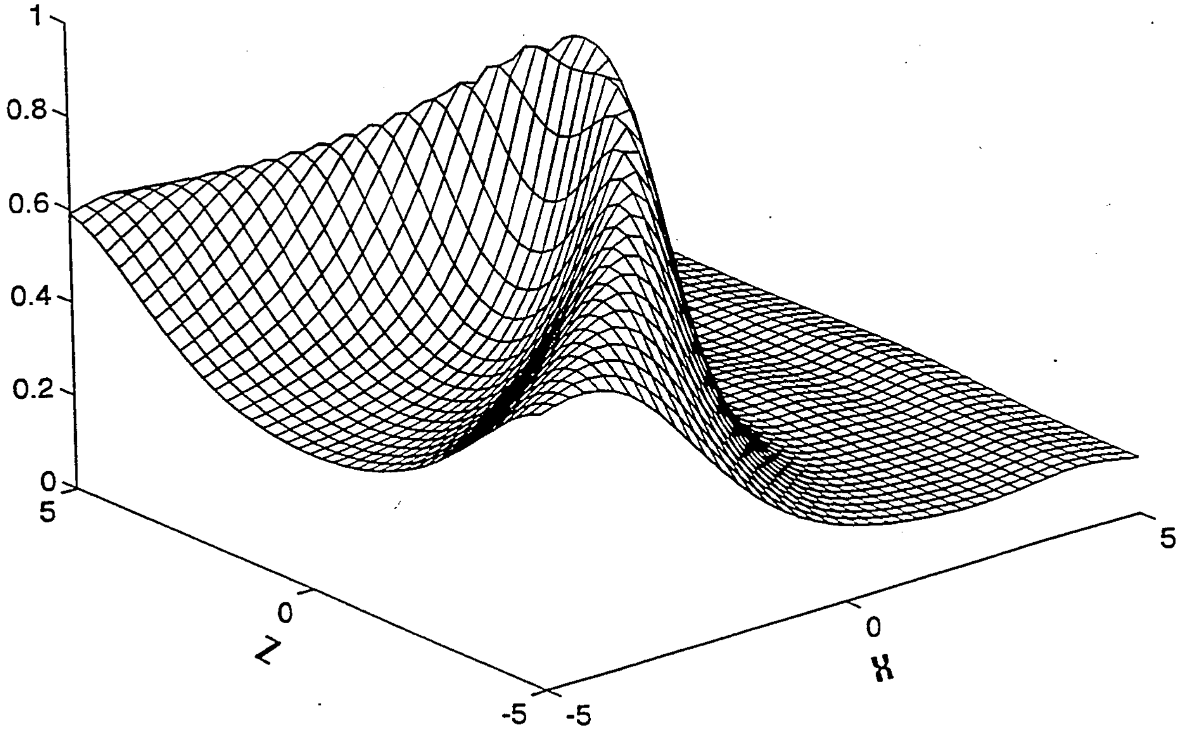

Figure 4.8. Normalized MUSIC Response in the x-z Plane for a Sensor Output SNR of 12 dB at 250 Hz. Maximum and Minimum Response Values Are 1.0 (x = -0.25, z = 0.0) and 0.12 (x = 5.0, z = -3.75)

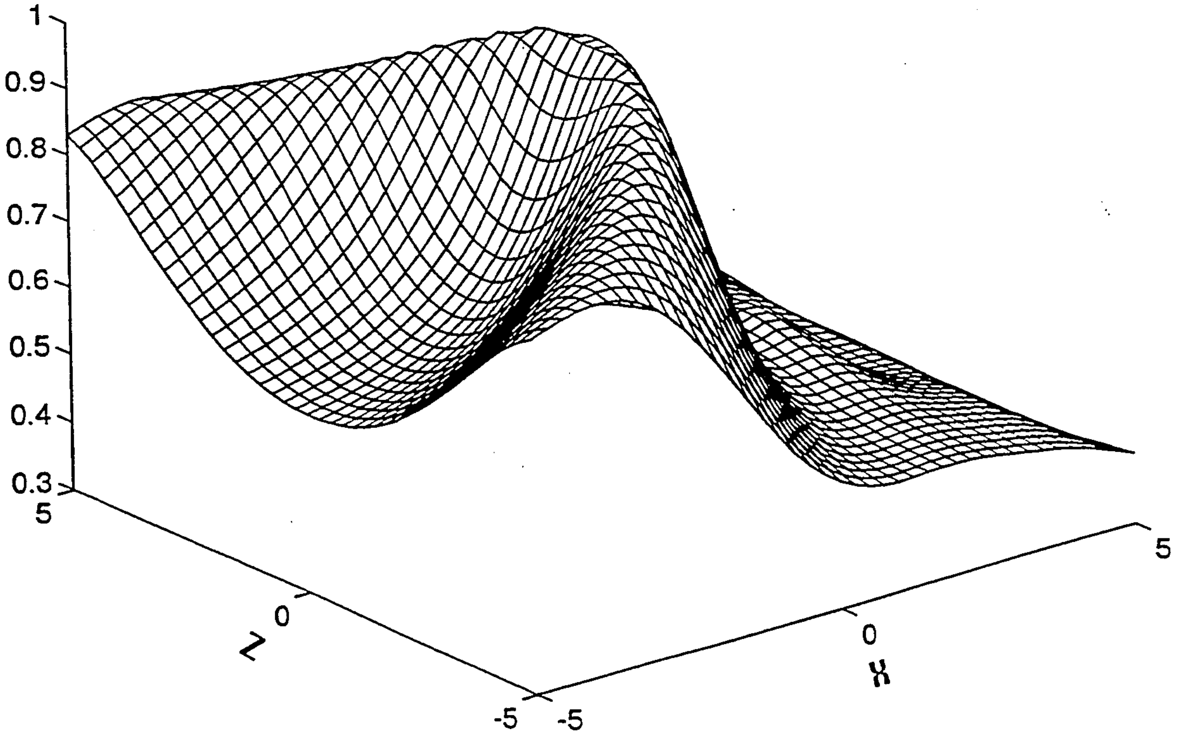

Figure 4.9. Normalized MAGDR Response in the x-z Plane for a Sensor Output SNR of 12 dB at 250 Hz. Maximum and Minimum Response Values Are 1.0 (x = -0.25, z = -0.5) and 0.362 (x = 5.0, z = -1.0)

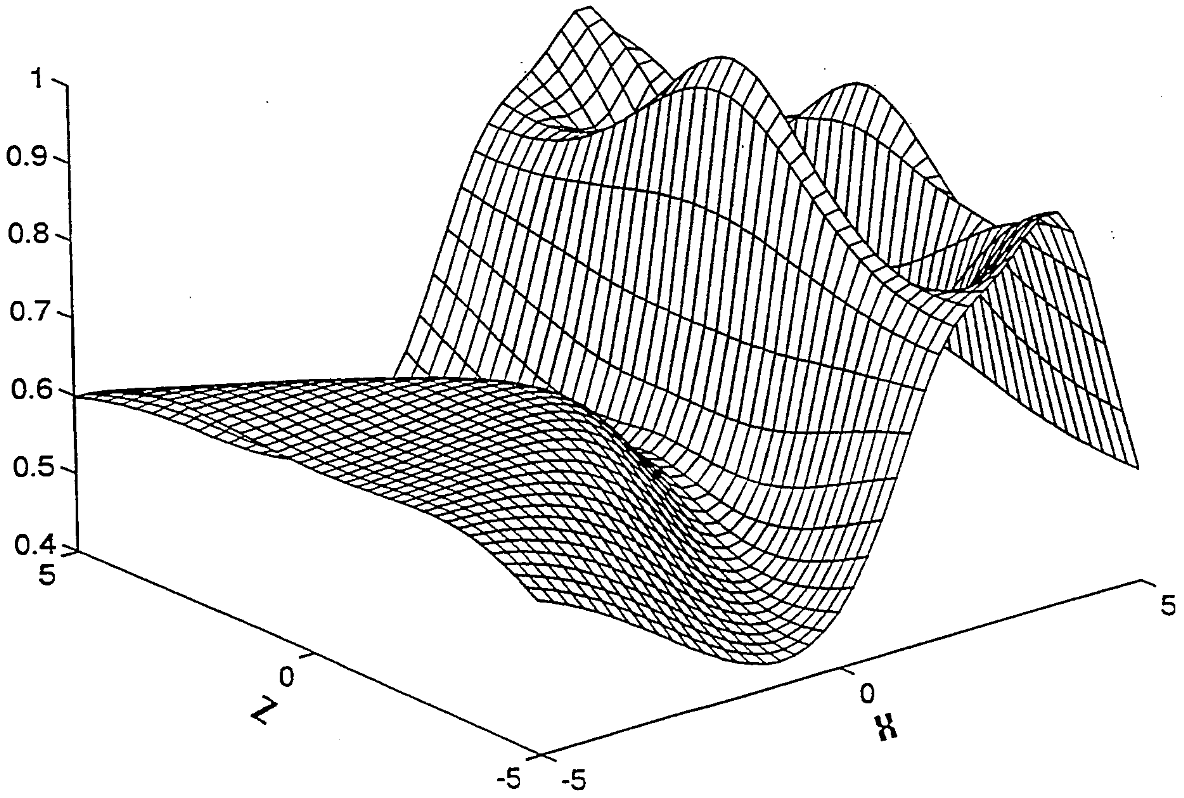

Figure 4.10. Normalized MUSIC Response in the x-z Plane for a Sensor Output SNR of 3 dB at 250 Hz. Maximum and Minimum Response Values Are 1.0 (x = 2.25, z = 0.0) and 0.431 (x = -1.0, z = -5.0)

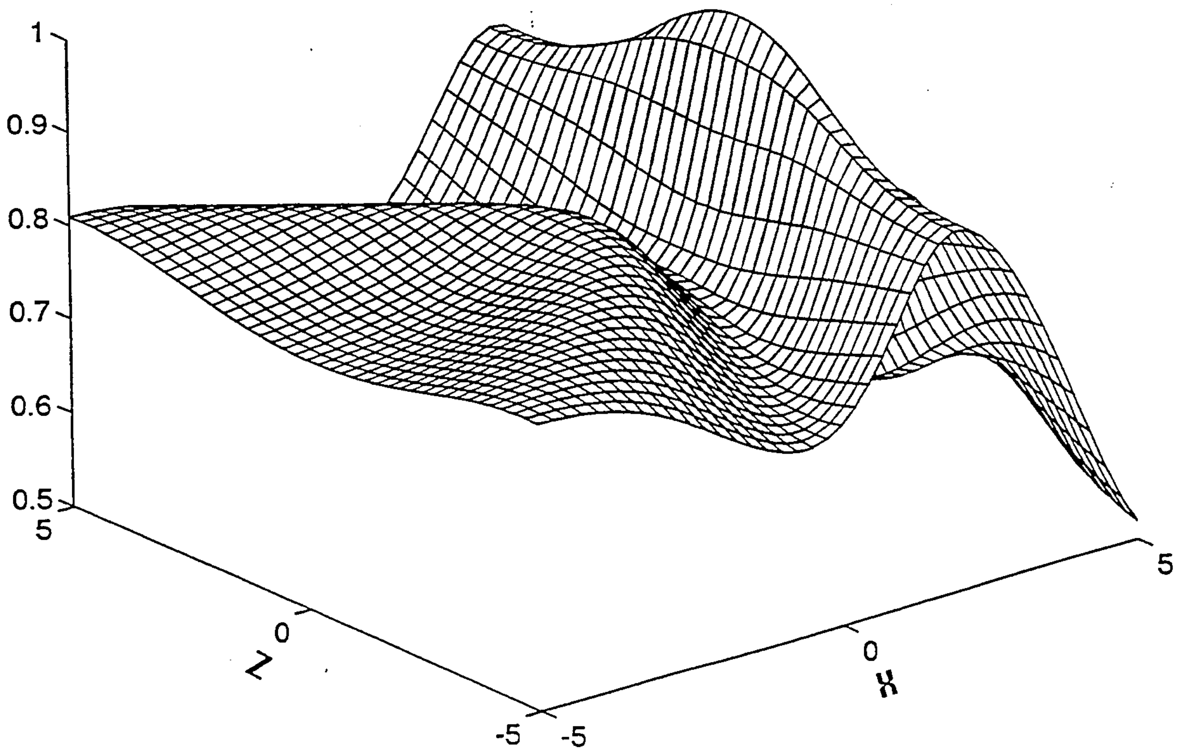

Figure 4.11. Normalized MAGDR Response in the x-z Plane for a Sensor Output SNR of 3 dB at 250 Hz. Maximum and Minimum Response Values Are 1.0 (x = 2.25, z = 0.0) and 0.5203 (x = 5.0, z = -5.0)

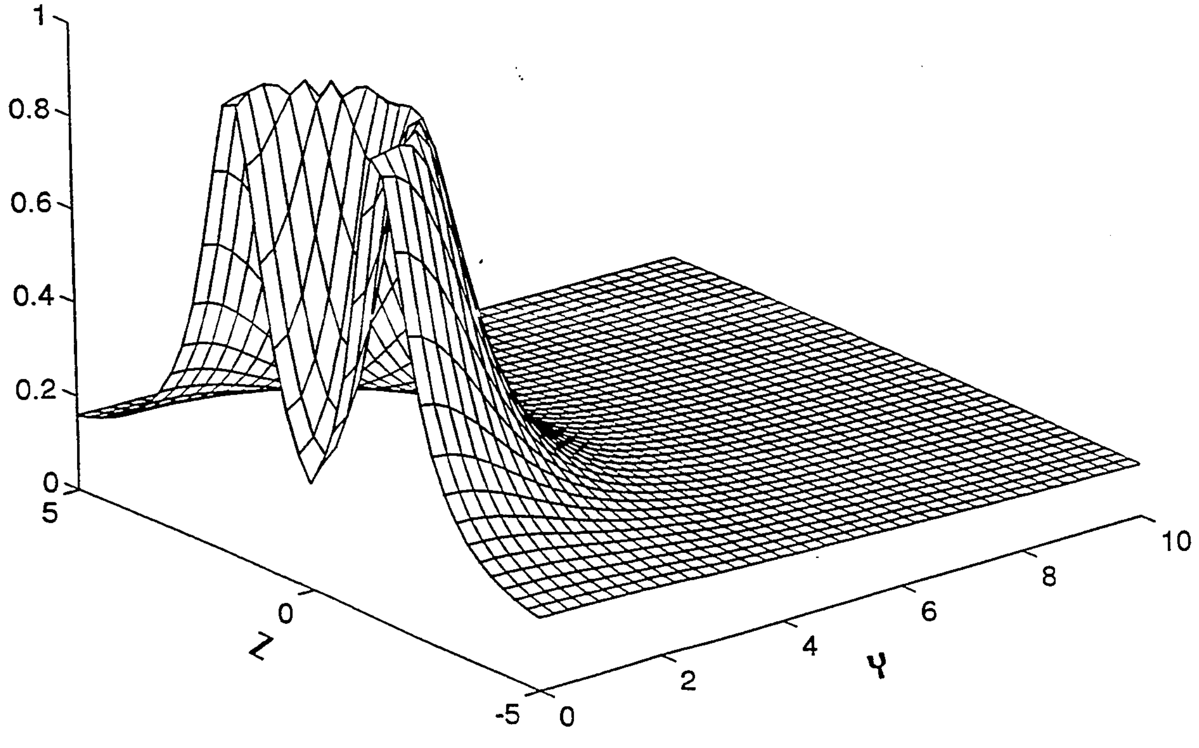

Figure 4.12. Normalized MUSIC Response in the y-z Plane for a Sensor Output SNR of 12 dB at 250 Hz. Maximum and Minimum Response Values Are 1.0 (y = 0.5, z = -1.5) and 0.113 (y = 10.0, z = -5.0)

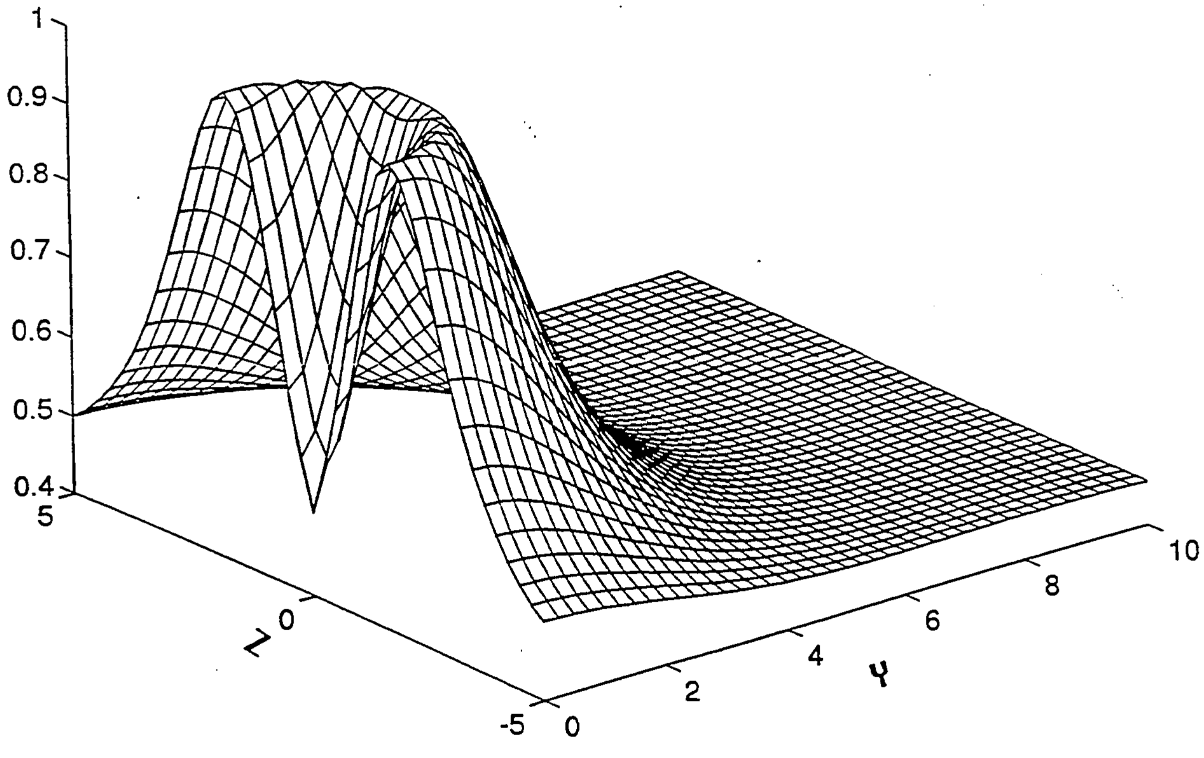

Figure 4.13. Normalized MAGDR Response in the y-z Plane for a Sensor Output SNR of 12 dB at 250 Hz. Maximum and Minimum Response Values Are 1.0 (y = 0.25, z = -1.7) and 0.4557 (y = 6.25, z = -4.5)

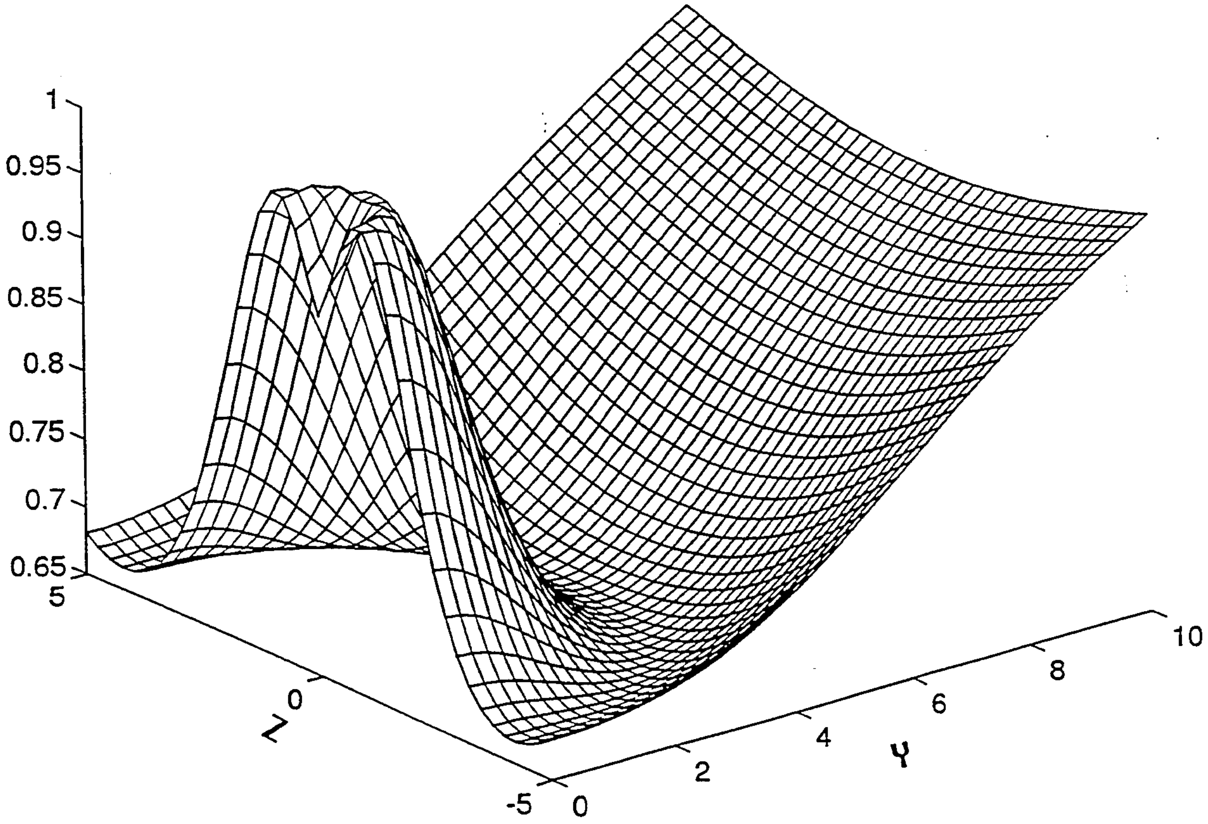

Figure 4.14. Normalized MUSIC Response in the y-z Plane for a Sensor Output SNR of 3 dB at 250 Hz. Maximum and Minimum Response Values Are 1.0 (y = 0.5, z = -0.75) and 0.6665 (y = 1.25, z = -4.0)

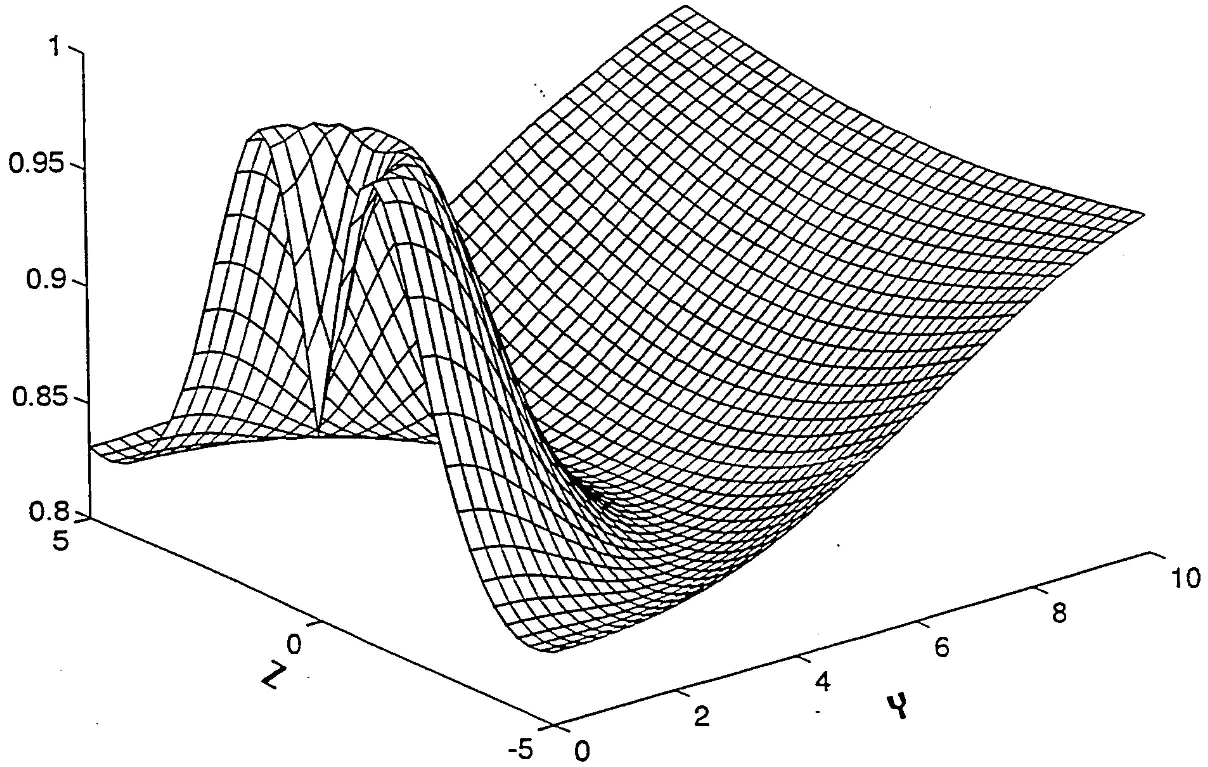

Figure 4.15. Normalized MAGDR Response in the y-z Plane for a Sensor Output SNR of 3 dB at 250 Hz. Maximum and Minimum Response Values Are 1.0 (y = 0.0, z = -1.25) and 0.8292 (y = 0.75, z = -4.5)

CHAPTER 5. CONCLUSIONS AND RECOMMENDATIONS

The results presented in this report show that the turbulent energy induced into a solid viscoelastic medium can be detected and that the energy can be resolved using a conventional beamformer. Additionally, simulation-based model predictions show that this type of source has significant potential for being localized and imaged. The laboratory experimental work should be expanded to measurements taken with background noises, nonhomogeneous media, advanced beamformers, and a sensor array rather than a series of two-point measurements. This approach will provide a better understanding of such issues as SNR, detection threshold, and human implementation.

In order for this type of detection, localization, and imaging to be executed in humans, the following technical issues will have to be resolved:

(a) *Transducer Phase Accuracy Requirements* - Array transducer location accuracy is absolutely essential. Such array geometry accuracy will likely dictate either a rigid or semirigid frame to which the transducers can be attached. It is envisioned that this frame can be suspended in a completely reusable exterior air bladder, which could be inflated, thereby forcing the sensor array to conform tightly to the patient's skin in order to maximize energy coupling and reduce impedance mismatch. Acoustic absorption at the rear of the bladder must be maximized to minimize reflected energy interference. This issue must be given the primary attention.

(b) *Signal and Masking Source Acoustic Power Levels Relative to the Statistically Uncorrelated Component of the Transducer Output* - The relative levels of the various signal sources and system noise with respect to the vibration sensing transducer pickup noise component, which is statistically uncorrelated between transducers, are major determinants of the extent to which desired waveforms can be extracted from the background noise and subsequently resolved spatially from other concurrent interfering sources.

(c) *Affected Artery Segments and Sources of Acoustic Masking Energy* - The limits of spatial resolution and the required complexity of the digital signal processing (DSP) hardware are determined by the angular extent of the particular distribution of the sources of energy. In addition, the spatial coherence of the extended source is significant. For example, the nonlinear (chaotic) nature of turbulent flow either through a stenotic valve or regurgitant valve would tend to be spatially incoherent, whereas the pressure field generated by the synchronized movement of points on a vessel wall, which is being excited to resonance by turbulent internal flow, may be spatially coherent.

(d) *Temporal Extent for Which Cycle-to-Cycle Acoustic Energy Can Be Coherently Integrated* - Energy field temporal coherence can be used to enhance high performance modern DSP algorithm capability if the received space-time field wave form can be synchronized from one heart cycle to the next.

(e) *Cost-Effective Hardware-Software Realization* - Modern high performance DSP algorithms are notably very computationally intense with regard to matrix (linear) algebra requirements. While arithmetically intensive, such matrix-vector computations are very amenable to efficient implementation on parallel architecture computing devices.

(f) *Homogeneity of the Sound Propagation Medium* - The capability to realize both a high SNR gain and high resolution is limited by the amount of uncertainty in the propagation time assumed from a point of focus either on or in the heart to each of the auscultation points. This propagation time is dependent on the degree of uniformity in material density along the propagation path. For example, fatty tissue would presumably be less dense than fluid and would therefore exhibit a slower propagation velocity. Moreover, the absorption and scattering of energy may complicate the vibration field beyond what can be easily modeled as straight-line propagation. This problem may require a complete and accurate solution to the wave equation within the torso, using the appropriate boundary conditions.

It should be explicitly noted that the energy sources are located in the very nearfield of the auscultation transducer array. Moreover, because of the proximity of source locations and the transducer array, the traditional radar/sonar assumption of a spatially stationary signal field with uniform spatial placement of the transducers in the array may be violated. This aspect of the problem eliminates from consideration the use of high performance locator algorithms, such as autoregressive (AR), autoregressive moving average (ARMA) (Akay, 1990) and ESPRIT (Owsley, 1985; Owsley, 1992). Specifically, the reduced rank minimum variance distortionless response (MVDR) beamfoming algorithm is a prime candidate for waveform extraction and the enhanced MVDR algorithm is a valid choice for the location of lesion-induced resonant points in the coronary artery mesh (Owsley, 1985; Owsley, 1992).

6. REFERENCES

Akay, M., Semmlow, J., Welkowitz, W., Bauer, M., and Kostis, J, "Detection of Coronary Occlusions Using Autoregressive Modeling of Diastolic Heart Sounds," *IEEE Transactions on Biomedical Engineering*, Vol. **37**/4, April 1990, pp. 366-373.

Akay, M., Akay, Y., Welkowitz, W., Semmlow, J., and Kostis, J., "Application of Adaptive Filters to Noninvasive Acoustical Detection of Coronary Occlusions Before and After Angioplasty," *IEEE Transaction on Biomedical Engineering*, Vol. **39**/2, February 1992, pp. 176-184.

Abiko, S., Kurokawa, Y., and Watanabe, K., "Noninvasive Detection of Intercranial Vascular Lesions by Recording Blood Flow Sounds," *Stroke*, Vol. **25**/2, February 1994, pp. 397-402.

Bendat, J. S., and Piersol, A. G., *Engineering Applications of Correlation and Spectral Analysis*, John Wiley & Sons, New York, 1980, pp. 9-12.

Bendat, J. S., and Piersol, A. G., *Random Data Analysis and Measurement Procedures*, John Wiley & Sons, New York, 1986, pp. 370-372.

Bradshaw, P., *An Introduction to Turbulence and Its Measurement*, Pergamon Press, New York, 1971, pp. 34-40.

Corcos, G. M., "Resolution of Pressure in Turbulence," *Journal of the Acoustical Society of America*, Vol. **35**, 1963, pp. 192-199.

Epstein, E., *Cardiac Auscultation*, Butterworth-Heinemann Ltd, Oxford, 1991, pp. 13-15.

Kassal, J., Reeves, W., and Donnerstein, R. L., "Polymer-Based Adherent Differential-Output Sensor for Cardiac Auscultation," *Medical Electronics*, September 1994, pp. 54-63.

Lees, R., and Kistler, J., "Carotid Phonoangiography," *Noninvasive Diagnostic Techniques in Vascular Disease*, A. Bernstein, Editor, St. Louis, MO, CV Mosby, 1978, pp. 187-194.

Metravib Instruments, *Metravib Viscoanalyseur User's Guide*, Limonest, France, 1989.

Owsley, N., Haykin, S., Kak, A., Chen, H., and Justice, J., *Array Signal Processing*, Prentice-Hall, Englewood Cliffs, NJ, 1985.

Owsley, N., Modern Space-Time Signal Processing, Advanced Technology Institute Short Course, copywrite 1987, latest revision November 1992.

Owsley, N., "A Space-Time Signal Processing Technique for the Detection, Location, and Analysis of Turbulent Blood Flow in Arteries," U.S. Navy Invention Disclosure Case No. 76365, 1 June 1994, New London, CT.

Smol'yakov, A. V., and Tkachenko, V. M., *The Measurement of Turbulent Fluctuations*, Springer-Verlag, Berlin, 1983, p. 24.

Verberg, J., "Transmissions of Vibrations of the Heart to the Chest Wall," *Advanced Cardiovascular Phys.*, Karger and Basel, Vol. 5 (Part III), 1983, pp. 84-103.

Wang, J., Tie, B., Welkowitz, W., Semmlow, J., and Kostis, J., "Modeling Sound Generation in Stenosed Coronary Arteries," *IEEE Transactions on Biomedical Engineering*, Vol. **37**/11 November 1990, pp. 1087-1094.

INITIAL DISTRIBUTION LIST

Addressee	No. of Copies
Defense Technical Information Center	12
Analysis and Technology (J. Kassal)	5
MedAcoustics Corporation (A. Eberhardt, M. Nixon)	2
Massachusetts General Hospital (R. Levine, M.D.)	1
Office of Naval Research (T. G. Goldsberry, K. Dial)	2